Effects of base flow modifications on noise amplifications: flow past a backward-facing step

X. M A O

School of Engineering and Computing Sciences, Durham University, Durham, DH1 3LE, UK

Amplifications of flow past a backward-facing step to optimal inflow and initial perturbations are investigated at Reynolds number 500. Two mechanisms of receptivity to inflow noise are identified: the bubble-induced inflectional point instability and the misalignment effect downstream of the secondary bubble. The further development of the misalignment results in decay of perturbations from $x = 28$ (the step is located at $x = 0$), as has been observed in previous non-normality studies (Blackburn *et al.* 2008), and eventually limits the receptivity. The receptivity is found to maximise at inflow perturbation frequency $\omega = 0.50$ and spanwise wavenumber $\beta = 0$, where the inflow noise takes full advantage of both mechanisms and is amplified over two orders in terms of the velocity magnitude. In direct numerical simulations (DNS) of the flow perturbed by optimal or random inflow noise, vortex shedding, flapping of bubbles, three-dimensionality and turbulence are observed in succession as the magnitude of the inflow noise increases. Similar features of linear and nonlinear receptivity are observed at higher Reynolds number. The Strouhal number of the bubble flapping is 0.08, at which the receptivity to inflow noise reaches maximum. This Strouhal number is close to reported values extracted from DNS or large eddy simulations at larger Reynolds number (Le *et al.* 1997; Kaiktsis *et al.* 1996; Métais 2001; Wee *et al.* 2004). Methodologies to further clarify the mechanisms of receptivity and suppress the noise amplifications by modifying the base flow using a linearly optimal body force is proposed. It is noticed that the mechanisms of optimal noise amplifications are fully revealed in the distribution of the base flow modification, which weakens the bubble instabilities and the misalignment effects and subsequently reduces receptivity significantly. Comparing the base flow modifications with respect to amplifications to inflow and initial perturbations, it is found that the maximum receptivity to initial perturbations is highly correlated with the receptivity to inflow noise at the optimal frequency $\omega = 0.50$ while the correlation reduces as the inflow frequency deviates from this optimal value.

1. Introduction

The flow past a backward-facing step is a canonical amplifier of noise originating from either the inflow boundary or the initial conditions. This noise amplification can be related with flow oscillations, e.g. vortex shedding (Kaiktsis & Monkewitz 2003), flapping of the separated shear layers (Schäfer *et al.* 2009) and three-dimensionality (Barkley *et al.* 2002), and subsequently leads to laminar-turbulence transition or structure fatigue (Mcgregor & White 1970). The noise amplification can be suppressed by modifying the base flow to be less sensitive to perturbations. Below the technique of base flow modifications is introduced in § 1.1 and the flow past a backward-facing step is reviewed in § 1.2.

1.1. *Base flow modifications*

Many basic flows, e.g. boundary layer flow, channel flow, flow past bluff bodies, vortex flow and so forth, either act as oscillators or noise amplifiers (Huerre & Monkewitz 1990). For oscillators which are asymptotically unstable to initial perturbations, it is possible to modify the base flow with small magnitude so as to change their asymptotic instability characteristics. This base flow modification investigation started from localized studies of incompressible flow, e.g. sensitivity analyses of eigenvalues of the Orr-Sommerfeld operator to modifications of the base flow (Bottaro *et al.* 2003) and optimal distortion of a base flow with a Hagen-Poiseuille profile to stabilise the most unstable modes of the locally defined linearised Navier-Stokes (NS) operator (Gavarini *et al.* 2004). These localised studies of variation on base flow velocity profiles in incompressible flow were extended to variation on velocity and density profiles in compressible flow by Lesshafft & Marquet (2010). The global counterpart of the effects of base flow variation on instabilities, which is the sensitivity of the most unstable global mode to variation of the base flow, has been investigated in the context of flow past a circular cylinder by Marquet *et al.* (2008*b*).

For amplifiers, which are commonly asymptotically stable but exhibits strong transient energy growth, the base flow variation with respect to the transient energy growth (amplification to the optimal initial perturbation) is more meaningful than to stabilities (amplification to the most unstable mode). Such base flow modifications to minimise/maximise the transient growth of the optimal initial perturbations have been conducted in the context of a flat-plate boundary layer flow, and it was found that a very weak modification of the base flow has a significant impact on the amplification of the Tollmien-Schlichting (TS) waves (Brandt *et al.* 2011).

The modification of the base flow can be achieved by a direct modification (Marquet *et al.* 2008*b*), blowing/suction imposed on the boundary (Lashgari *et al.* 2014), adding a body force to the governing equations (Brandt *et al.* 2011) and so forth. The body force can be, to name a few, Lorenz force generated by electrodes and magnets mounted in a solid body (Zhang *et al.* 2010) or hydrodynamic force generated by a small cylinder introduced into the domain. This "small control cylinder" exerts a force on the base flow which is opposite to its drag, and has been shown to be effective in suppressing vortex shedding downstream of a cylinder as experimentally investigated by Strykowski & Sreenivasan (1990) and numerically studied by Giannetti & Luchini (2007).

Most of these previous studies on base flow modifications concentrated on the evolution of initial perturbations either in the form of the most unstable modes or optimal initial perturbations. However for base flow acting as noise amplifiers, the initial perturbations will be convected out of the domain after a long enough time interval and therefore the receptivity to temporally continuous inflow/free-stream noise may be more appropriate than initial perturbations to describe the dynamics of this type of base flow. Most of the existing studies on receptivity to boundary noise focused on the response of the base flow to prescribed boundary disturbances in the form of free-stream noise or wall roughness and the connection between free-stream noise and instabilities or laminar-turbulence transition (Schrader *et al.* 2009; Zaki *et al.* 2010). The optimal boundary perturbation, or the most energetic perturbation over a given time horizon, has been calculated in the form of wall-normal disturbances in a locally defined swept Hiemenz flow (Guégan *et al.* 2006) and in a boundary layer flow (Cathalifaud & Luchini 2000). These local studies on optimal boundary perturbations have been extended to the global scope to calculate the global optimal inflow perturbation to stenotic flow (Mao *et al.* 2012) and vortex flow (Mao *et al.* 2013).

In the current work, the technique of base flow modifications and the concept of global

optimal receptivity to boundary perturbations are combined to calculate the variation of a base flow that maximises/minimises its optimal receptivity to boundary noise, referring to the maximum gain stemming from the most energised boundary perturbation, rather than the gain of an empirically prescribed boundary perturbation or random noise. The base flow modification with respect to receptivity to initial perturbations will be also calculated for comparison. It will be shown that besides shedding lights to the control of noise amplifications, the base flow modification study also helps to clarify the noise amplification mechanisms.

1.2. *Flow past a backward-facing step*

The flow past a backward-facing step has been extensively studied and established as a benchmark of computational fluid dynamics. In stability analyses, the two-dimensional flow was reported to be absolutely stable up to a Reynolds number of at least $Re = 600$ and convectively unstable for at least $Re > 525$ (Kaiktsis *et al.* 1996). The dependence of instabilities on the expansion ratio has been studied and centrifugal instability, elliptic instability and lift-up mechanisms are identified when reducing the expansion ratio from 0.972 to 0.25 (Lanzerstorfer & Kuhlmann 2012). In the current work, the Reynolds number is defined using the upstream centreline velocity and the step height and all cited results are converted to this definition. For $Re > 748$, the flow loses stability to steady perturbations with spanwise wavenumber 0.91 owing to the centrifugal instability mechanism and becomes three-dimensional (Barkley *et al.* 2002). The three-dimensionality in flow past a backward-facing step has been also attributed to side-wall effects, shear layer instabilities or inflow noise (Armaly *et al.* 1983; Kaiktsis *et al.* 1996; Yanase *et al.* 2001; Barkley *et al.* 2002). In the current work, the periodic boundary condition implemented in the spanwise direction excludes the influence of the side-wall, and it will be shown that the three-dimensionality can be activated by the receptivity to inflow perturbations.

Apart from the asymptotic instabilities, the transient energy growth of initial perturbations has been thoroughly investigated in the asymptotically stable condition at $Re = 500$ (Blackburn *et al.* 2008). The transient growth has been found to be responsible for the laminar-turbulent transition (Boiko *et al.* 2012), while in the current investigation, it is observed that the laminar-turbulent transition can be triggered by receptivity to inflow noise, whose mechanism is similar with the nonmodal transient growth.

For flow oscillations in the region downstream of the step, e.g. vortex shedding and flapping of the bubbles, acoustic radiations have been reported to be a possible mechanism in compressible flow (Yokoyama *et al.* 2007). For incompressible flow, Wee *et al.* (2004) found that at $Re = 5550$, the Strouhal number of the self-sustained vortex shedding is $St = O(0.1)$, which matches the frequency of the linearly most unstable mode, indicating a correlation between linear instabilities and the vortex shedding. By perturbing the inlet velocity profile, Le *et al.* (1997) observed a quasi-periodic oscillation of the recirculation length with $St \approx 0.06$ at $Re = 7650$. In large eddy simulations (LES) of the full turbulent flow, Métais (2001) obtained a Strouhal number $St = 0.07$ for the oscillation of the primary reattachment length. These reported Strouhal numbers are close to that of the most amplified inflow perturbation calculated in the current work at a relatively low Reynolds number $Re = 500$. In another study of the correlation of the frequency of the inflow noise with the oscillation of the flow, Kaiktsis *et al.* (1996) observed that the flow unsteadiness strongly depends on selective sustained external excitation with even small amplitudes at $525 \leq Re \leq 1875$. In DNS at $Re = 4500$, Schäfer *et al.* (2009) found that the vortical structures associated with vortex shedding are responsible for the flapping of the separation lines and reattachment lines of the primary and secondary bubbles. In

the current work, the generation of the vortical structures between the main stream and the bubbles is investigated so as to identify the source of vortex shedding and flapping.

Receptivity of the flow past a backward-facing step to inflow noise has been widely observed. High sensitivity of the flow downstream of the step with respect to the type of inflow boundary conditions has been reported (Kaltenbach & Janke 2000; Schäfer *et al.* 2009) and strong correlations between the frequency of the inflow noise and the oscillation of the shear layers downstream of the step were observed (Kaiktsis *et al.* 1996). It has been argued that the combination of inflow disturbances and shear layer instabilities, e.g. Kelvin-Helmholtz instabilities, triggers the three-dimensional vortical structures (Yanase *et al.* 2001). However, in all these works, the distribution of the inflow noise is either empirically prescribed or random, while in the current work, the optimal (most energetic) inflow perturbation will be calculated and the relation of the optimal inflow perturbation with vortex shedding, flapping of the bubbles and three-dimensionality will be explored.

Control of the flow past a backward-facing step using blowing/suction or geometry variations, which can be interpreted as base flow modifications, has been discussed mostly in attempts to enhance noise amplifications. A combination of suction on the step face and blowing downstream of the step has been used to destabilise the flow and enhance mixing in the channel (Kaiktsis & Monkewitz 2003). It was also suggested that the destabilised two-dimensional flow is subject to three-dimensional secondary instabilities. Similar destabilisation and enhancement of mixing was obtained by modulating the flow using spanwise distributed roughness elements upstream of the step (Boiko *et al.* 2012) or tabs on the edges of the step (Park *et al.* 2007). These previous control or base flow modification studies all aim at activating instabilities and turbulence, while in the current work, the base flow modification generated by the linearly optimal body force can either suppress or enhance the noise amplifications depending on the choice of a scale factor that measures the size and sign of the body force.

The remainder of this paper is organised as follows. In § 2, the methodology to calculate the optimal base flow modification induced by the body force is demonstrated; then after a convergence test in § 3, the receptivity of flow past a backward-facing step to inflow noise is presented in § 4; the optimal modification of the base flow with respect to the receptivity is further studied in § 5; the correlation between receptivities to inflow and initial perturbations is discussed in § 6; finally conclusions are drawn in § 7.

2. Methodology

In this section, the methodology to calculate the body force that (in the linear regime) optimally modify the base flow and subsequently its amplification to optimal boundary or initial perturbations is presented. The perturbations and their developments are modelled in § 2.1; the definitions of noise amplifications are presented in § 2.2; a Lagrangian functional is defined in § 2.3; based on this Lagrangian, the formulation of the optimal body force is derived in § 2.4; finally the calculation procedure is summarised in § 2.5.

2.1. *Governing equations*

For the flow past a backward-facing step, assuming the fluid to be incompressible, the governing equations, i.e. the incompressible NS equations, can be written as

$$\partial_t \hat{\boldsymbol{u}} + \hat{\boldsymbol{u}} \cdot \boldsymbol{\nabla} \hat{\boldsymbol{u}} + \boldsymbol{\nabla} \hat{p} - Re^{-1} \nabla^2 \hat{\boldsymbol{u}} = \boldsymbol{f} \quad \text{with} \quad \boldsymbol{\nabla} \cdot \hat{\boldsymbol{u}} = 0,$$

where Re is the Reynolds number defined using the maximum inflow velocity and the step height and $Re = 500$ is used throughout this work, $\hat{\boldsymbol{u}}$ is the velocity vector, $\hat{p}$ is the kinematic pressure and $\boldsymbol{f}$ denotes the body force. On the inflow boundary, appropriate

Dirichlet velocity conditions (a perturbed parabolic profile in this work) are imposed as will be described in detail in the following, on the wall boundary, no-slip velocity conditions are adopted, and on the outflow boundary, zero Dirichlet and zero Neumann conditions are implemented for the velocity and pressure terms respectively. A computed Neumann pressure condition is adopted if the velocity boundary condition is of Dirichlet-type (Karniadakis *et al.* 1991). These equations are compactly written as

$$\partial_t \hat{\boldsymbol{u}} + D\hat{\boldsymbol{u}} = \boldsymbol{f} \tag{2.1}$$

in the following, where D is a nonlinear operator, whose linear counterpart has been well used in hydrodynamic stability analyses, as will be presented in the following.

At $Re = 500$, the flow past a backward-facing step is a strong noise amplifier (Blackburn *et al.* 2008) and therefore the solution of the NS equations can be unsteady if perturbations, e.g. initial perturbations, boundary perturbations or external forcing, are introduced to the computational domain. However, by integrating the NS equations over a long enough time period to "wash out" the initial perturbations and specifying a zero body force and an appropriate steady inflow boundary condition, e.g. a parabolic velocity profile, a steady solution can be obtained. Such a steady solution, denoted as the base flow in the following, is subject to perturbations, e.g. boundary perturbations and initial perturbations. Therefore the "real" flow can be decomposed as the sum of the base flow and the perturbation flow, i.e. $(\hat{\boldsymbol{u}}, \hat{p}) = (\boldsymbol{U}, P) + (\boldsymbol{u}, p)$, where $(\boldsymbol{U}, P)$ denote the base flow velocity and pressure respectively and $(\boldsymbol{u}, p)$ represent the perturbation velocity and pressure respectively.

If the magnitude of the perturbation is small compared with the base flow, the development of perturbations is governed by the linearised NS equations:

$$\partial_t \boldsymbol{u} + \boldsymbol{U} \cdot \boldsymbol{\nabla} \boldsymbol{u} + (\boldsymbol{\nabla} \boldsymbol{U})^T \cdot \boldsymbol{u} + \boldsymbol{\nabla} p - Re^{-1} \nabla^2 \boldsymbol{u} = 0 \quad \text{with} \quad \nabla \cdot \boldsymbol{u} = 0,$$

or more compactly as

$$\partial_t \boldsymbol{u} - L(\boldsymbol{U})\boldsymbol{u} = 0, \tag{2.2}$$

where $L(\boldsymbol{U})$ is the linearised operator of D, depending on the base flow and acting on the perturbation. This operator has been extensively explored in stability and non-normality studies (Trefethen *et al.* 1993; Chomaz 2005; Schmid 2007). The boundary conditions for the linearised NS equations are the same as those for the NS equations (2.1), except that on the inflow boundary, a velocity perturbation is imposed after decomposing the unperturbed parabolic profile from the perturbed inflow velocity condition.

The perturbations may stem from either boundary perturbations or initial perturbations. The initial perturbation can be modelled as the initial condition of the linearised NS equations, denoted as $\boldsymbol{u}_0$. Correspondingly the boundary perturbation can be modelled as the boundary condition of the linearised NS equations, denoted as $\boldsymbol{u}_b(\boldsymbol{x}, t)$, where $\boldsymbol{x}$ represents the coordinate of the perturbation boundary. To reduce the dimension of $\boldsymbol{u}_b(\boldsymbol{x}, t)$ after temporal-spatial discretisation, decompose the temporal and spatial dependence as

$$\boldsymbol{u}_b(\boldsymbol{x}, t) = \tilde{\boldsymbol{u}}_b(\boldsymbol{x}) T(t, \omega) \tag{2.3}$$

where $\tilde{\boldsymbol{u}}_b(\boldsymbol{x})$ is the spatial dependence and $T(t, \omega)$ is a prescribed temporal-dependence function,

$$T(t, \omega) = (1 - e^{-\sigma t^2})[1 - e^{-\sigma(\tau - t)^2}]e^{i\omega t}, \tag{2.4}$$

where τ is a final time, σ is a positive relaxation factor, the first two factors ensure $\boldsymbol{u}_b(\boldsymbol{x}, 0) = 0$ and $\boldsymbol{u}_b(\boldsymbol{x}, \tau) = 0$ in order to eliminate the temporal and spatial discontinuity at the beginning of the integration of the linearised NS equations and the adjoint equation

(will be introduced later in (2.9)), and the last factor specifies the frequency of the inflow perturbation as ω when the final time tends to infinity. It is seen that for increasing σ, $T(t, \omega) \to e^{i\omega t}$. However a large value of σ induces high gradient of $T(t, \omega)$ or $\boldsymbol{u}_b(\boldsymbol{x}, t)$ with respect to t at $t = 0$ and therefore leads to numerical discontinuity. The choice of this relaxation factor will be discussed in detail in § 3. In the current work, the inflow boundary is considered as the perturbation boundary so as to model the upstream noise. Under the linear assumption that the perturbations are small enough, the developments of the boundary and initial perturbations are decoupled and therefore can be considered separately.

To simplify notation, introduce scalar products

$$(\boldsymbol{a}, \boldsymbol{b}) = \int_\Omega \boldsymbol{a} \cdot \boldsymbol{b} \, dV, \qquad \langle \boldsymbol{a}, \boldsymbol{b} \rangle = \tau^{-1} \int_0^\tau (\boldsymbol{a}, \boldsymbol{b}) dt \qquad \text{and} \qquad [\boldsymbol{c}, \boldsymbol{d}] = \int_{\partial \Omega_b} \boldsymbol{c} \cdot \boldsymbol{d} \, dS,$$

where Ω represents the spatial domain, $\partial \Omega_b$ denotes the perturbation boundary, referring to the inflow boundary in the current work, $\boldsymbol{a}$ and $\boldsymbol{b}$ are defined on the domain Ω, and $\boldsymbol{c}$ and $\boldsymbol{d}$ are defined on the perturbation boundary $\partial \Omega_b$.

2.2. Receptivity to inflow and initial perturbations

The receptivity of the base flow to inflow perturbations can be quantified as the gain

$$K \equiv \max_{\tilde{\boldsymbol{u}}_b} \frac{(\boldsymbol{u}_\tau, \boldsymbol{u}_\tau)}{[\tilde{\boldsymbol{u}}_b, \tilde{\boldsymbol{u}}_b]}, \tag{2.5}$$

where $\boldsymbol{u}_\tau$ denotes the perturbation velocity at the final time. From the definition, the gain K represents the largest amplification of the base flow to all possible inflow boundary perturbations for a given final time and inflow frequency. The boundary perturbation at which K is obtained is referred to as the optimal boundary perturbation. In this definition, the initial perturbation is set to zero. The methodology to calculate K and the associated optimal boundary perturbation has been addressed in Mao *et al.* (2013).

Correspondingly the receptivity to initial perturbations or transient energy growth can be quantified by the gain

$$G \equiv \max_{\boldsymbol{u}_0} \frac{(\boldsymbol{u}_\tau, \boldsymbol{u}_\tau)}{(\boldsymbol{u}_0, \boldsymbol{u}_0)}, \tag{2.6}$$

where G represents the maximum ratio of the final energy and the initial energy over the time period considered. The initial perturbation at which the gain G is obtained is the optimal initial perturbation. In this definition, the boundary perturbations are set to zero. The methodology to calculate G and the optimal initial perturbation has been well established (Barkley *et al.* 2008) and applied to flow past a backward-facing step (Blackburn *et al.* 2008).

2.3. Lagrangian functional for base flow modifications

To investigate effects of base flow modifications on noise amplifications, variation techniques are implemented (Bottaro *et al.* 2003; Schmid 2007; Marquet *et al.* 2008*b*; Brandt *et al.* 2011). Define the Lagrangian functional as

$$\mathcal{L} = \text{gain} - \langle \boldsymbol{u}^*, \partial_t \boldsymbol{u} - L(\boldsymbol{U})\boldsymbol{u} \rangle + (\boldsymbol{\lambda}, D\boldsymbol{U} - \boldsymbol{f}), \tag{2.7}$$

where the gain is K for boundary perturbation studies and G for initial perturbation studies, as defined in (2.5) and (2.6) respectively; the second term is a constraint that the perturbation satisfies the linearised NS equations and $\boldsymbol{u}^*$ is the adjoint velocity; the third term is the constraint that the base flow satisfies the steady NS equations and λ is a Lagrangian multiplier. It is worth noting that the last term involves the nonlinear

NS equations, which will be linearised when calculating the linear sensitivity of the Lagrangian functional with respect to the base flow. This nonlinear form is adopted to facilitate the identification of nonlinear saturation of the body force effects, which involves solving the nonlinear forced NS equations. From the definition of the nonlinear operator D (see Eqn. 2.1) and the linear operator L (see Eqn. 2.2), it is noted that the divergence free conditions for the base flow $\boldsymbol{U}$ and perturbation $\boldsymbol{u}$ have been imposed as constraints in this Lagrangian functional. For boundary perturbation studies the initial perturbation is set to zero while for initial perturbation studies, the boundary perturbation is zero.

One may integrate the second term by parts to obtain

$$\mathcal{L} = \text{gain} + \langle \boldsymbol{u}, \partial_t \boldsymbol{u}^* + L^*(\boldsymbol{U})\boldsymbol{u}^* \rangle - (\boldsymbol{u}_\tau, \boldsymbol{u}_\tau^*) + (\boldsymbol{u}_0, \boldsymbol{u}_0^*) + [g(\boldsymbol{u}^*), \tilde{\boldsymbol{u}}_b] + (\boldsymbol{\lambda}, D\boldsymbol{U} - \boldsymbol{f}), \tag{2.8}$$

where L^* is the adjoint operator of L and

$$\partial_t \boldsymbol{u}^* + L^*(\boldsymbol{U})\boldsymbol{u}^* = 0 \tag{2.9}$$

represents the adjoint equation, which has been extensively used in non-normality studies and can be expanded as

$$\partial_t \boldsymbol{u}^* + \boldsymbol{U} \cdot \boldsymbol{\nabla}\boldsymbol{u}^* - \boldsymbol{\nabla}\boldsymbol{U} \cdot \boldsymbol{u}^* - \boldsymbol{\nabla}p^* + Re^{-1}\nabla^2\boldsymbol{u}^* = 0 \qquad \text{with} \qquad \boldsymbol{\nabla} \cdot \boldsymbol{u}^* = 0.$$

It is noticed that this adjoint equation is integrated backwards in time (Barkley *et al.* 2008). $\boldsymbol{u}_\tau^*$ and $\boldsymbol{u}_\tau$ denote the adjoint velocity at $t = \tau$ and $t = 0$ respectively. $g(\boldsymbol{u}^*)$ can be calculated by integrating the adjoint equation as

$$g(\boldsymbol{u}^*) = \tau^{-1} \int_0^\tau (p^*\boldsymbol{n} - Re^{-1}\boldsymbol{\nabla_n}\boldsymbol{u}^*)T(t, -\omega)\,\mathrm{d}t, \tag{2.10}$$

where $\boldsymbol{\nabla_n} = \boldsymbol{n} \cdot \boldsymbol{\nabla}$, with $\boldsymbol{n}$ denoting the unit outward normal on the boundary. In this derivation, the inflow and wall boundary conditions for the adjoint velocity are set to zero; on the outflow, Robin velocity and zero Dirichlet pressure conditions are adopted (Mao *et al.* 2013).

2.4. *Linearly optimal body force*

The base flow can be modified directly or by a body force added in the NS equations (Brandt *et al.* 2011). A directly modified flow may violate the divergence free condition while the body-forced modification, obtained by integrating the forced NS equations, reserves the divergence free condition. Therefore in the current work, the base flow modification is generated by the body force, whose optimal (most effective in modifying the base flow and its noise amplification characteristics) distribution can be calculated through evaluating the gradient of the Lagrangian with respect to the body force.

Setting to zero the first variations of $\mathcal{L}$ with respect to $\boldsymbol{u}^*$, $\boldsymbol{u}$ and λ, it is obtained that the perturbation, adjoint and base flow variables satisfy the linearised NS, adjoint and NS equations respectively. Since the adjoint equation is integrated backwards, its initial condition is $\boldsymbol{u}_\tau^*$, which can be obtained by setting the first variation of $\mathcal{L}$ to $\boldsymbol{u}_\tau$ to zero:

$$\boldsymbol{u}_\tau^* = \frac{2\boldsymbol{u}_\tau}{[\tilde{\boldsymbol{u}}_b, \tilde{\boldsymbol{u}}_b]} \qquad \text{or} \qquad \boldsymbol{u}_\tau^* = \frac{2\boldsymbol{u}_\tau}{(\boldsymbol{u}_0, \boldsymbol{u}_0)}, \tag{2.11}$$

for boundary perturbation and initial perturbation problems respectively.

At the equilibrium state, where the Lagrangian reaches maximum, for receptivity to inflow boundary perturbations, $\boldsymbol{u}_0$ is zero and $\tilde{\boldsymbol{u}}_b$ is the optimal boundary perturbation and parallel with $g(\boldsymbol{u}^*)$ (Mao *et al.* 2012), as can be obtained by setting the variation with respect to $\tilde{\boldsymbol{u}}_b$ to zero. Correspondingly, for receptivity to initial perturbations, $\tilde{\boldsymbol{u}}_b$ is

zero and $\boldsymbol{u}_0$ is parallel with $\boldsymbol{u}_0^*$, as can be obtained by setting the variation with respect to $\boldsymbol{u}_0$ to zero.

Considering the Gâteaux differential as presented by Guégan *et al.* (2006), the gradient of the Lagrangian with respect to the body force is $\nabla_{\boldsymbol{f}}\mathcal{L} = \boldsymbol{\lambda}$. Since the original body force used to calculate the base flow is zero (unforced), a linearly optimal body force which is most effective in modifying the receptivity is,

$$\boldsymbol{f} = 0 + r\frac{\nabla_{\boldsymbol{f}}\mathcal{L}}{(\nabla_{\boldsymbol{f}}\mathcal{L}, \nabla_{\boldsymbol{f}}\mathcal{L})^{1/2}} = r\frac{\boldsymbol{\lambda}}{(\boldsymbol{\lambda}, \boldsymbol{\lambda})^{1/2}}, \tag{2.12}$$

where r is a scale factor of the body force and r^2 represents the square integration of the body force in the computational domain. Therefore the modified base flow obtained by driving the NS equations with the optimal body force can be considered as a function of r.

Setting the variation of the Lagrangian to the base flow $\boldsymbol{U}$ to zero, it is seen that $\boldsymbol{\lambda}$ satisfies

$$L^*(\boldsymbol{U})\boldsymbol{\lambda} = \boldsymbol{F} \tag{2.13}$$

where

$$\boldsymbol{F} = \tau^{-1}\int_0^\tau (-\nabla\boldsymbol{u} \cdot \boldsymbol{u}^* + \boldsymbol{u} \cdot \nabla\boldsymbol{u}^*)\mathrm{d}t/[\tilde{\boldsymbol{u}}_b, \tilde{\boldsymbol{u}}_b]. \tag{2.14}$$

In this derivation, a term in $\boldsymbol{F}$ involving integration over all the boundaries, that is $-\int \boldsymbol{u}^*\boldsymbol{u}\cdot\boldsymbol{n}\mathrm{d}S$, is dropped. This term is zero on the wall boundaries and inflow boundaries, but may not vanish on the outflow boundaries. Since $\boldsymbol{F}$ can be interpreted as the gradient of the Lagrangian with respect to the base flow (without constraint of satisfying the NS equations), by further restricting the base flow modification to be inside the domain, this term turns to zero. As will be seen in the following sections, the base flow modification concentrates around the bubbles and is zero on the outflow boundary, confirming that this term can be dropped. Adopting another more complex form of the Lagrangian functional (see appendix A), this term also vanishes, and the same result of the body force can be obtained.

Since the base flow is constraint to be steady, the body force $\boldsymbol{f}$, and consequently $\boldsymbol{\lambda}$, should be also steady. Therefore $\boldsymbol{\lambda}$ can be calculated as the steady solution of the forced adjoint equation

$$\partial_t\boldsymbol{\lambda} + L^*(\boldsymbol{U})\boldsymbol{\lambda} = \boldsymbol{F}. \tag{2.15}$$

2.5. *Calculation procedure*

The procedure to calculate the optimal base flow modification with respect to receptivity to inflow noise can be summarised as:

(*a*) Calculate the unforced base flow $\boldsymbol{U}$ from the NS equations (2.1) with $\boldsymbol{f} = 0$.

(*b*) Compute the optimal boundary perturbation to the unforced base flow (Mao *et al.* 2013).

(*c*) Integrate the linearised NS equations (2.2) and adjoint equation (2.9) to obtain $\boldsymbol{u}(t)$ and $\boldsymbol{u}^*(t)$ and calculate the force $\boldsymbol{F}$ using (2.14).

(*d*) Integrate the forced adjoint equation (2.15) backwards over a long enough time until obtaining a steady solution of $\boldsymbol{\lambda}$.

(*e*) Substitute $\boldsymbol{\lambda}$ into (2.12) and choose a scale factor r for the body force to obtain a linearly optimal body force $\boldsymbol{f}$.

(*f*) Substitute the optimal body force $\boldsymbol{f}$ into the NS equations (2.1) and integrate over long enough time until reaching a steady forced solution.

P	grid	Δt	K
3	A	0.004	6.407×10^5
4	A	0.004	6.147×10^5
5	A	0.004	6.090×10^5
6	A	0.004	6.112×10^5
7	A	0.004	6.113×10^5
5	B	0.004	6.113×10^5
5	A	0.002	6.095×10^5

TABLE 1. Convergence of the optimal gain K with respect to the polynomial order P in the spectral element method, the grid and the time step Δt. The parameters are Reynolds number $Re = 500$, final time $\tau = 150$, spanwise wavenumber $\beta = 0$ and temporal frequency for inflow perturbation $\omega = 0.5$, as will be used in all the following convergence tests if not otherwise stated.

For initial perturbation problems, step (b) should be replaced as computing the optimal initial perturbations and all the following steps are the same.

The difference between the forced base flow and the unforced base flow can be interpreted as the base flow modification due to the linearly optimal body force. Then effects of optimal base flow modifications on receptivity can be verified by comparing the gain K (or G) based on the forced and unforced base flows.

3. Discretisation and validation

Spectral elements employing nodal-based polynomial expansions within quadrilateral elemental subdomains are adopted for the two-dimensional spatial discretisation combined with a Fourier decomposition in the spanwise direction. Time integration is carried out using a velocity-correction scheme. Details of the discretisation and its convergence properties (exponential in spatial variables, second-order in time) are given in Blackburn & Sherwin (2004). The same numerics are used to solve the NS, linearised NS and adjoint equations.

The computational domain and grid consisting of 992 spectral elements are shown in Fig. 1. The step is located at $x = 0$, the outflow length (measured from the step to the outflow boundary) is 50, identical to the configuration used in a previous non-normality study (Blackburn *et al.* 2008). The inflow boundary is located at $x = -5$, which results in a shorter inflow length (measured from the inflow boundary to the step) than that used in Blackburn *et al.* (2008), in order to isolate the step-induced dynamics from the upstream channel-induced dynamics. The inflow boundary is adopted as the perturbation boundary without the most upper and lower edges since these two edges are connected to the upper or lower wall, where no inflow noise should be introduced. Therefore the perturbation boundary is at $x = -5$ and $0.06 \leq y \leq 0.94$.

In all the convergence investigations conducted in this section, a large final time $\tau = 150$ is adopted to eliminate transient effects. The frequency and spanwise wavenumber of the boundary perturbation are set to $\omega = 0.5$ and $\beta = 0$, where the gain K reaches maximum as will be discussed later in Fig. 4.

Convergence of the discretisation is tested with respect to the spectral element decomposition and the polynomial order P used in nodal expansions in each spectral element. Two grids are studied: grid A as illustrated in Fig. 1 and grid B with the same domain but 2317 spectral elements. The relaxation factor σ defined in (2.4) is set to $\sigma = 1$ in these convergence tests and it has been observed that a further increase of σ changes the
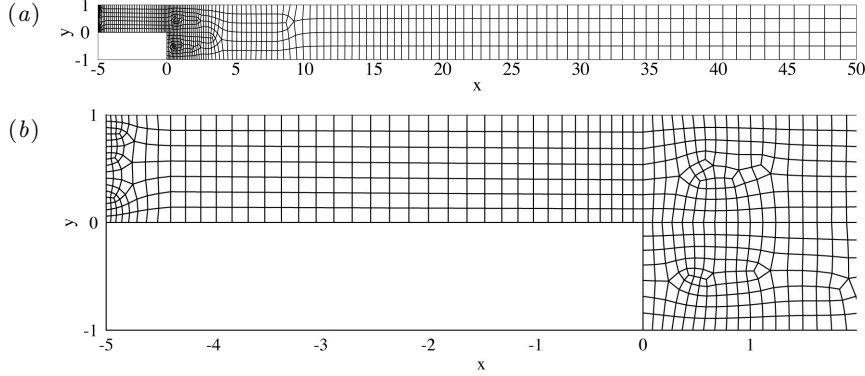
FIGURE 1. Spectral elements in the computational domain: (a) overall domain and (b) domain close to the inflow boundary and the step.
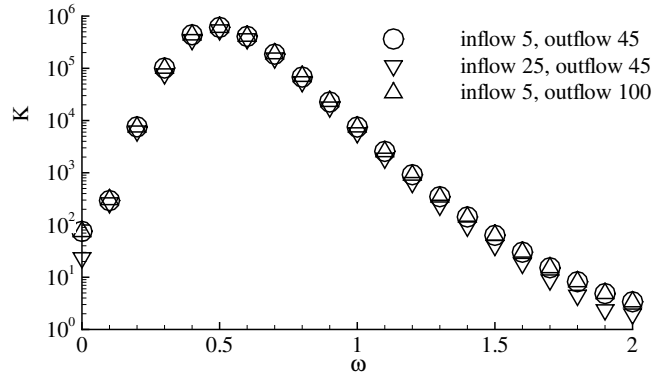

FIGURE 2. Convergence of the gain with respect to the domain size.

magnitude of noise amplifications slightly for final time $\tau < 70$, at which the transient growth is evident, and has negligible effects for $\tau > 70$. As most of the following work focuses on large final time at which the transient effect vanishes, i.e. $\tau = 150$, $\sigma = 1$ is used throughout this work. As shown in Table 1, the gain K converges to relative error less than 0.4% at $P = 5$ and grid A for further refinements of the spatial discretisation. It is also seen in Table 1 that when the time step Δt is halved from 0.004 to 0.002, the relative change of K is less than 0.3%. Therefore in all the following integrations of the NS, linearised NS and adjoint equations, grid A is adopted with polynomial order $P = 5$ and time step $\Delta t = 0.004$.

Computational grids with longer inflow and outflow sections are generated to check the dependence of the gain on the domain size, as shown in Fig. 2. It is observed that the gain converges well with respect to the outflow length, and does not vary significantly with respect to the inflow length around the optimal frequency, i.e. $\omega = 0.5$. At higher frequencies, the inflow perturbation is more diffused in the inflow channel and therefore a longer inflow section reduces the gain K.

The convergence of the optimal body force and the outcome of the optimal inflow perturbation is presented in Table 2, while the distribution of the optimal inflow perturbation will be discussed later in Fig. 5. The body force at extended domains, denoted as $\boldsymbol{f}_i$, is projected to the one at the default domain (inflow length 5 and outflow length 50), represented as $\boldsymbol{f}_1$, so as to use the convergence of $(\boldsymbol{f}_i, \boldsymbol{f}_1)/\sqrt{(\boldsymbol{f}_1, \boldsymbol{f}_1)(\boldsymbol{f}_i, \boldsymbol{f}_i)}$ to 1

Case	inflow length	outflow length	$(\boldsymbol{f}_i, \boldsymbol{f}_1)/\sqrt{(\boldsymbol{f}_1, \boldsymbol{f}_1)(\boldsymbol{f}_i, \boldsymbol{f}_i)}$	$(\boldsymbol{u}_{\tau i}, \boldsymbol{u}_{\tau 1})/\sqrt{(\boldsymbol{u}_{\tau 1}, \boldsymbol{u}_{\tau 1})(\boldsymbol{u}_{\tau i}, \boldsymbol{u}_{\tau i})}$
1	5	50	1	1
2	15	50	0.99911	0.98049
3	25	50	0.99908	0.98024
4	5	80	0.99910	0.98994
5	5	100	0.99918	0.98976

TABLE 2. Convergence of the optimal body force $\boldsymbol{f}$ and the optimal outcome $\boldsymbol{u}_\tau$ with respect to the inflow and outflow lengths. The subscript i denotes the ith case, e.g. $\boldsymbol{f}_1$ is the optimal body force for case 1.
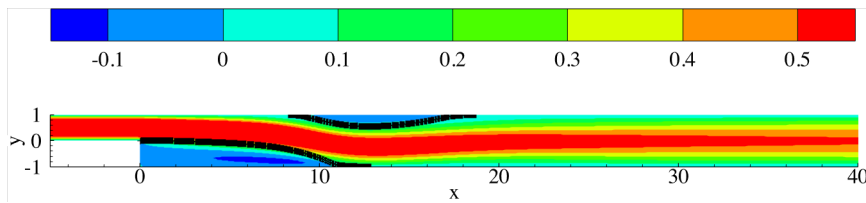
FIGURE 3. Contours of the streamwise velocity component of the base flow. Thick solid lines represent the border streamlines of recirculation bubbles. The Reynolds number is fixed at $Re = 500$ for this and all the following plots if not otherwise stated.

as the indication of the similarity of the two body forces. It is seen that this indicator deviates from 1 within the discretization error for the four extended domains considered, suggesting that the optimal body force, which is the main focal of this work, is independent on further extensions of the domain. Similarly it is noticed that a longer outflow or inflow section does not change the distribution of the optimal outcome $\boldsymbol{u}_\tau$ significantly, as indicated by the value of $(\boldsymbol{u}_{\tau i}, \boldsymbol{u}_{\tau 1})/\sqrt{(\boldsymbol{u}_{\tau 1}, \boldsymbol{u}_{\tau 1})(\boldsymbol{u}_{\tau i}, \boldsymbol{u}_{\tau i})}$, where $\boldsymbol{u}_{\tau i}$ and $\boldsymbol{u}_{\tau 1}$ denote the outcome at extended and default domains respectively.

4. Receptivity to inflow perturbations

The receptivity of the flow past a backward-facing step is studied first before addressing the base flow modifications. Since the receptivity to initial perturbations in the backward-facing step flow has been thoroughly studied but the receptivity to inflow noise has received limited attention, in this section, the receptivity to inflow perturbations is investigated. In § 4.1, the optimal gain and the corresponding optimal inflow perturbation are presented; in § 4.2, the mechanisms of receptivity are revealed; in § 4.3, the nonlinear development of the optimal inflow perturbation is studied; in § 4.4, the random inflow noise is adopted to identify the role of optimal inflow perturbations in real conditions; finally in § 4.5, the dependence of receptivity on Reynolds number is presented.

4.1. *Optimal inflow perturbation and its outcome*

The unforced base flow ($\boldsymbol{f} = 0$) is illustrated in Fig. 3. Two recirculation bubbles, characterised by negative streamwise velocity, can be observed downstream of the step. The primary bubble is associated with the lower wall and reattaches around $x = 11$ while the secondary bubble is associated with the upper wall, separates around $x = 8$ and reattaches around $x = 17$. It is noticed that the flow is almost parallel downstream of the secondary bubble, which supports local, or streamwise periodic, perturbation devel-
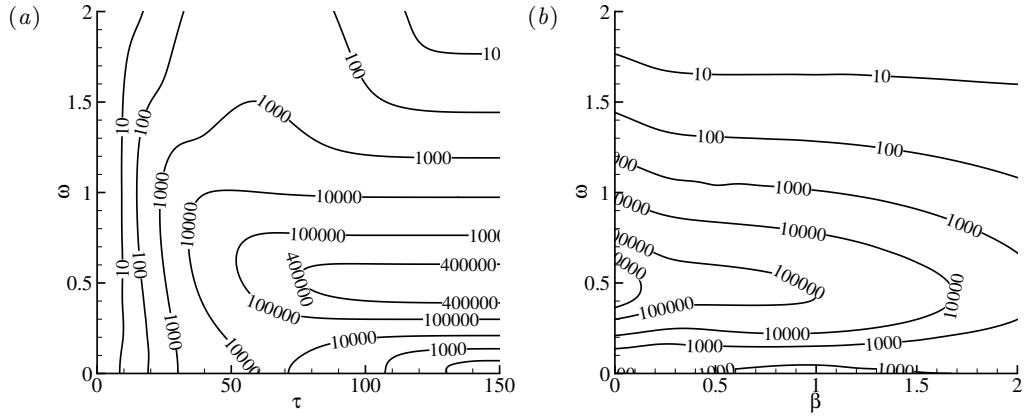
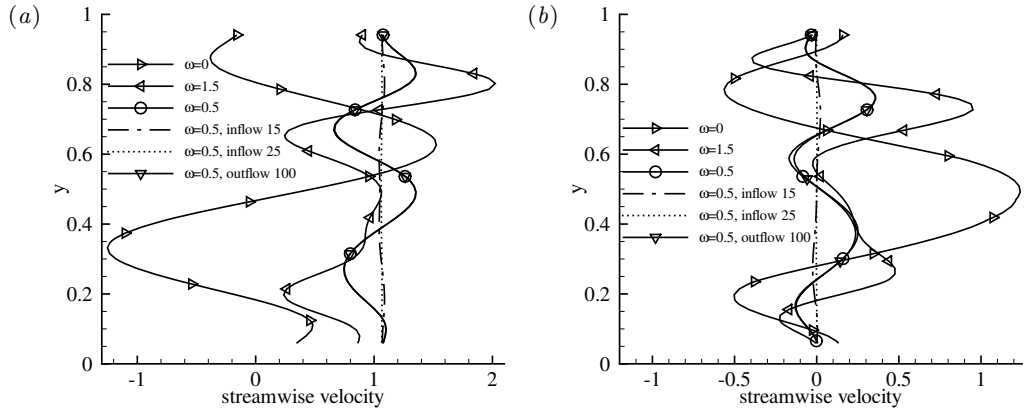FIGURE 4. Contours of the gain K at (a) $\beta = 0$ and (b) $\tau = 150$.

FIGURE 5. Distribution of the optimal inflow velocity $\tilde{\boldsymbol{u}}_b$ at $\tau = 150$ and $\beta = 0$. (a) Streamwise velocity component and (b) vertical velocity component. The magnitude is normalised to satisfy $[\tilde{\boldsymbol{u}}_b, \tilde{\boldsymbol{u}}_b] = 1$. The default inflow and outflow lengths are 5 and 50 respectively.

opments. This base flow is asymptotically stable but acts as an amplifier to upstream noise and exhibits strong transient energy growth (Blackburn *et al.* 2008; Marquet *et al.* 2008*b*).

The receptivity of this base flow to upstream noise, measured by the gain K, at various spanwise wavenumber β, final time τ and frequency ω is shown in Fig. 4. It is seen that inflow perturbations with $\omega = 0.50$ are the most amplified and the global maximum gain over the parameters considered appears at $\tau = 150$, $\beta = 0$ and $\omega = 0.50$. From the transient receptivity at $\beta = 0$ as revealed in Fig. 4(a), it is observed that the transient effects vanish at $\tau = 150$ (the gain becomes constant with respect to τ). Since the transient noise amplification can be clearer illustrated in receptivity to initial perturbations, for all the following studies of receptivity to inflow noise, $\tau = 150$ will be used if not otherwise stated in order to exclude transient effects. In Fig. 4(b), it is observed that the receptivity maximises at $\beta = 0$ and almost reduces monotonically for increasing β, except that at small ω, the optimal value of β is around 1.

In Fig. 5, the spatial distributions of the optimal inflow perturbation obtained at $\beta = 0$, $\tau = 150$ and three typical frequencies are displayed. It is noted that the vertical wavenumber of the perturbation increases while the oscillation magnitude reduces for
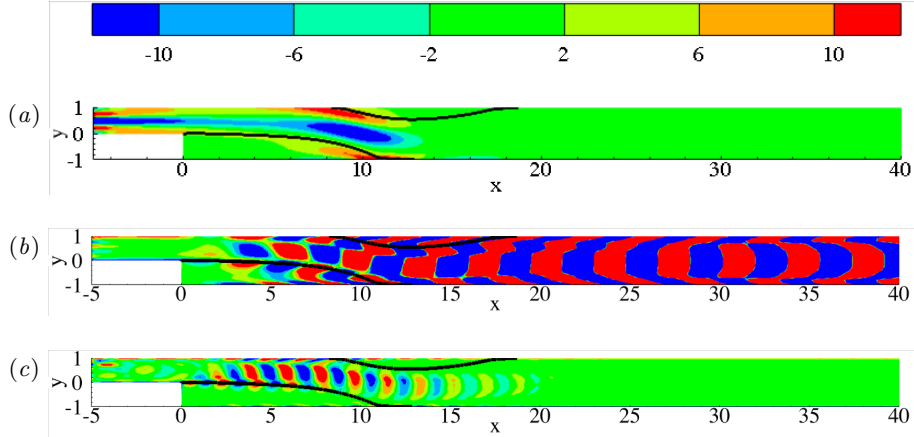
FIGURE 6. Contours of spanwise vorticity of the outcome of the optimal inflow boundary perturbation at $t = 150$, $\beta = 0$, $\tau = 150$ and (a) $\omega = 0$, (b) $\omega = 0.5$ and (c) $\omega = 1.5$. The inflow perturbation is normalized so that $[\tilde{\boldsymbol{u}}_b, \tilde{\boldsymbol{u}}_b] = 1$. Thick solid lines represent the borders of recirculation bubbles.

increasing ω. For the global optimal inflow perturbation ($\omega = 0.5$), the vertical component is significantly smaller than the streamwise component and therefore this global optimal perturbation can be interpreted as a streamwise gust. It is also worth noting that the distribution of the optimal inflow noise is independent on further extensions of the outflow section, while for a longer inflow section, it tends to be a uniform streamwise perturbation. Such a uniform inflow noise becomes optimal because it induces perturbations around the step with the same magnitude (considering the continuity and streamwise momentum equations), without being diffused in the elongated channel flow upstream of the step.

Fig. 6 reveals the outcome of the optimal inflow perturbations presented in Fig. 5. Since the distribution of the outcome is independent on the domain size as shown in Table 2, the optimal outcomes at various domain sizes are not presented here. The wavenumber of the perturbation in the streamwise direction roughly reflects the frequency of the inflow noise. It is worth noting that the outcome of the most energetic inflow perturbation at $\omega = 0.5$ is concentrated in the region downstream of the secondary bubble, with the magnitude of the inflow perturbation velocity amplified over two orders, while the outcomes at $\omega = 0$ and 1.5 are associated with the primary bubble and the fore part of the secondary bubble. For the three outcomes, the structures upstream of the end of the secondary bubble are dominated by strings of vorticity whose sign changes around the bubble borders and therefore manifests the inflectional point instability associated with shear layers in recirculation bubbles (Marquet *et al.* 2008*a*). For the two non-zero frequency cases, induced perturbations with smaller magnitudes around the upper and lower walls are also observed.

4.2. *Mechanisms of receptivity*

To illustrate the mechanism of receptivity, consider the case with $\beta = 0$, $\tau = 150$ and $\omega = 0.5$, where the receptivity maximises, as an example. From the momentum equation of perturbations, there is

$$\partial_t \frac{\boldsymbol{u} \cdot \boldsymbol{u}}{2} + \boldsymbol{\nabla} \cdot (\boldsymbol{U} \frac{\boldsymbol{u} \cdot \boldsymbol{u}}{2}) + \boldsymbol{u} \cdot \boldsymbol{\nabla}\boldsymbol{U} \cdot \boldsymbol{u} + \boldsymbol{\nabla} \cdot (\boldsymbol{u}p) = 0. \tag{4.1}$$

In this derivation, the viscous diffusion is neglected and the divergence free conditions of both the perturbation flow and base flow are used.
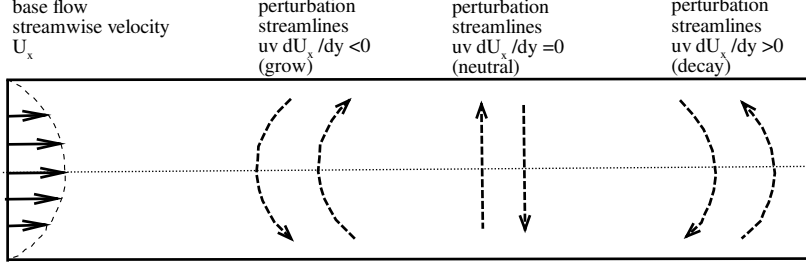
FIGURE 7. Perturbation streamlines that result in energy growth and decay in a parallel base flow. Solid lines with arrow denote the base flow streamwise velocity, dashed lines with arrow represent streamlines of the perturbation. The dotted line is the centre line of the channel while solid lines without arrow represent the border of a segment of the domain taken into account.

In the region downstream of the secondary bubble, the base flow is almost parallel (see Fig. 3). Neglecting the vertical component of the base velocity and the streamwise gradient of the streamwise base velocity, there is

$$\boldsymbol{u} \cdot \boldsymbol{\nabla} U \cdot \boldsymbol{u} = uv \frac{\mathrm{d}U}{\mathrm{d}y}, \tag{4.2}$$

where u, v and U are the streamwise perturbation velocity, vertical perturbation velocity and streamwise base velocity respectively.

It is also noted that in the region downstream of the secondary bubble, the perturbations are approximately periodic in the streamwise direction (see Fig. 6b), manifesting the local dynamics. Therefore the integration of the second and fourth terms in (4.1) over a section of the domain covering a period of the perturbations vanishes:

$$\int \boldsymbol{\nabla} \cdot (\boldsymbol{U} \frac{\boldsymbol{u} \cdot \boldsymbol{u}}{2} + \boldsymbol{u}p)\mathrm{d}V = \int \boldsymbol{n} \cdot (\boldsymbol{U} \frac{\boldsymbol{u} \cdot \boldsymbol{u}}{2} + \boldsymbol{u}p)\mathrm{d}S = 0, \tag{4.3}$$

since the velocities are zero on the wall boundary and are the same on the inflow and outflow boundaries of the selected domain, whose surface normal $\boldsymbol{n}$ is opposite.

Combining (4.1), (4.2) and (4.3), the energy equation of perturbations is obtained:

$$\mathrm{d}E/\mathrm{d}t = - \int uv \frac{\mathrm{d}U}{\mathrm{d}y}\mathrm{d}V, \tag{4.4}$$

similarly as presented in a vortex flow in a cylindrical frame (Pradeep & Hussain 2006). $E = \int \boldsymbol{u} \cdot \boldsymbol{u}/2\mathrm{d}V$ denotes the perturbation energy in this region, whose streamwise extension covers one period of the perturbations.

On the upper part of the channel, $\mathrm{d}U/\mathrm{d}y < 0$ whilst on the lower part, $\mathrm{d}U/\mathrm{d}y > 0$. Therefore a perturbation with left-headed streamlines (bends to the left) results in $uv\mathrm{d}U/\mathrm{d}y < 0$ and energy growth according to (4.4), a perturbation with right-headed streamlines (bends to the right) corresponds to $uv\mathrm{d}U/\mathrm{d}y > 0$ and decays in time, and a rectangular streamline is neutral (neither grows nor decays provided that viscous diffusion is neglected), as shown in Fig. 7.

From Fig. 6(b), it is seen that in the region around $x = 10$, where the primary bubble and the secondary bubble coexist, the perturbation vortex structures can be depicted as a combination of five vortex strings, as schematically plotted in Fig. 8. The main vortex string is between the two bubbles; owing to the bubble induced inflectional point instabilities, another two strings with opposite sign, denoted as bubble vortices, are generated around the bubble borders; the interaction of the dominant string of vortices with the
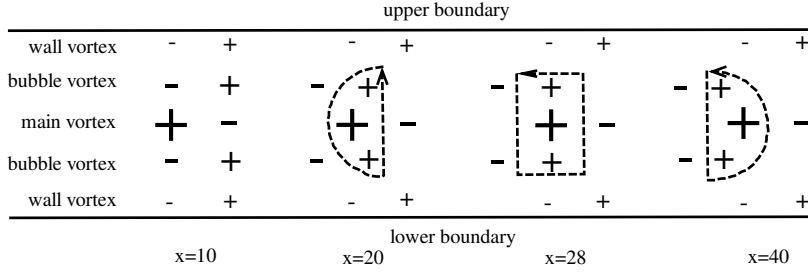
FIGURE 8. Sketch of vortex structures in the outcome of the optimal inflow perturbation at $\beta = 0$, $\tau = 150$ and $\omega = 0.5$ (see Fig. 6*b*).

wall boundary layer induces another two vortex strings around the upper and lower walls, denoted as wall vortices. In this region, the vortex structures are associated with instability mechanisms and so the five vortex strings are well aligned in the direction normal to the bubble border (shown as vertically distributed in Fig. 8 to facilitate comparison with downstream structures).

However, in the region downstream of the secondary bubble, where the bubble instability vanishes, the bubble vortices are no longer aligned with the dominant vortices. In this region, when the whole vortex structures are convected downstream by the base flow, the dominant vortices move faster than the bubble vortices, since the dominant vortices are located in the middle of the channel, where the base flow streamwise velocity maximises. Therefore the dominant vortices and bubble vortices form left-headed structures or streamlines at around $x = 20$, approximately rectangular profiles at $x = 28$ and finally right-headed structures at around $x = 40$, as shown in both Fig. 8 and Fig. 6(*b*). However the wall vortices always align with the main vortices since they are induced by the dominant vortices and are not affected by the convection effects. This transfer of streamline patterns from left-headed to rectangular and further to right-headed structures can be also observed in a previous non-normality work, with the neutral rectangular profile appearing also at around $x = 28$ (Blackburn *et al.* 2008).

Combining Fig. 6(*b*), 7 and 8, it can be summaries that the inflow perturbation is firstly amplified by the bubble induced inflectional point instabilities, further strengthened by the convection effects, which generate perturbations with left-headed (energy grow) streamlines, and then self-limited by the base flow convection, which eventually transfers the perturbations to be right-headed structures (energy decay). Therefore the perturbation magnitude grows upstream of the (neutral) rectangular streamlines, which are located at around $x = 28$, and decay downstream of this location. This threshold point for perturbation developments is not obvious in Fig. 6(*b*) owing to the choice of contour levels but can be seen clearer in a later discussion about developments of the optimal initial perturbation in Fig. 23. This amplification effect associated with base flow convection will be denoted as the misalignment mechanism in the following.

This mechanism also explains the receptivity at other frequencies. For the $\omega = 0$ case, there is no alternative vorticity and the misalignment mechanism does not appear, suggesting that the receptivity only relies on the bubble instabilities as shown in Fig. 6(*a*). At higher frequencies, e.g. $\omega = 1.5$, only the primary bubble induces instabilities and the secondary bubble instability is not activated, as shown in Fig. 6(*c*). Therefore the misalignment effects start downstream of the primary bubble and owing to the relatively short streamwise wavelength of the perturbation, the right-headed streamlines can be generated faster and appear even upstream of the end of the secondary bubble. Therefore
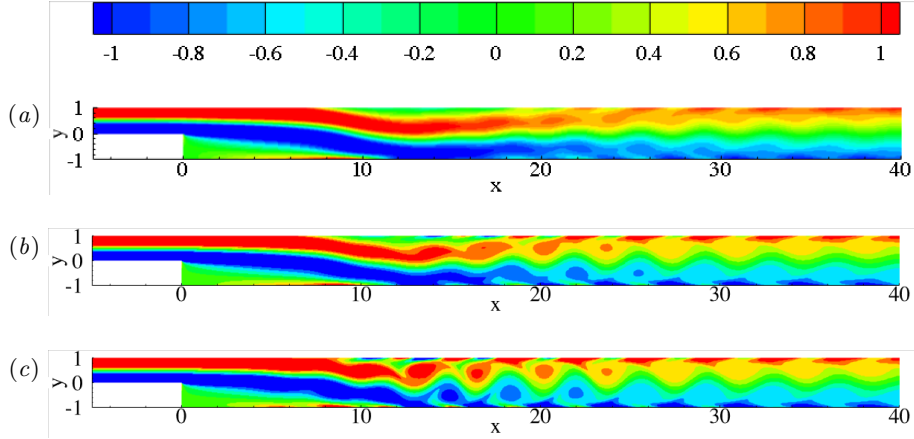
FIGURE 9. Contours of spanwise vorticity of flow perturbed by the optimal inflow perturbation at $\beta = 0$, $\omega = 0.5$ and $\tau = 150$. The magnitude of the inflow perturbation is $s = 0.0002$, 0.001 and 0.005 for (a), (b) and (c) respectively.

neither the bubble instability nor the misalignment mechanism is fully exploited in this case.

4.3. *Nonlinear development of the optimal inflow perturbations*

The receptivity presented above is about the linearised development of perturbations. In this subsection, the linear assumption is released and the magnitude of the boundary perturbation is introduced to study the development of the perturbed flow, which can be interpreted as the nonlinear evolution of the perturbations, through direct numerical simulations (DNS). The numerical setup is the same as in the calculation of the base flow except that the inflow velocity is perturbed by the optimal inflow perturbation:

$$\hat{\boldsymbol{u}}_{\text{in}} = \boldsymbol{U}_{\text{in}} + \frac{s}{[\tilde{\boldsymbol{u}}_b, \tilde{\boldsymbol{u}}_b]^{1/2}} \tilde{\boldsymbol{u}}_b T(t, \omega) \tag{4.5}$$

where the subscript "in" denotes the inflow boundary, $\boldsymbol{U}_{\text{in}}$ represents the parabolic steady velocity condition used to calculate the base flow, T is a temporal function as defined in (2.4), $\tilde{\boldsymbol{u}}_b$ is the global optimal inflow boundary perturbation obtained at $\omega = 0.5$, $\tau = 150$ and $\beta = 0$ and s denotes the magnitude of the inflow perturbation. To capture the complex fluid dynamics in the nonlinear development of the optimal inflow perturbation, a denser grid consisting of 2317 spectral elements is adopted in this subsection.

In the spanwise direction, periodic boundary conditions are implemented. The flow past a backward-facing step was reported to lose stabilities at $Re = 748$ to three-dimensional waves with spanwise wavenumber $\beta = 0.91$ (Barkley *et al.* 2002) while reach maximum three-dimensional transient energy growth at $\beta = 0.645$ (Blackburn *et al.* 2008). Therefore to roughly accommodate both the three-dimensional instabilities and optimal transient energy growth, the spanwise domain length is set to $L = 20.9$ and 64 Fourier modes are calculated with spanwise wavenumbers 0, 0.3, 0.6, 0.9, ..., 18.9.

Five typical values of s are tested: 0.0002, 0.001, 0.005, 0.01 and 0.02. The perturbed flow is stable to three-dimensional perturbations for the first three s and becomes three-dimensional for the last two. For the first three s, the two-dimensional perturbed flow is illustrated in Fig. 9. It is seen that as s increases, the vortex shedding point moves upstream, since the perturbation is gradually amplified and maximises at around $x = 28$ when convected downstream. At $s = 0.0002$, where the inflow velocity perturbation is
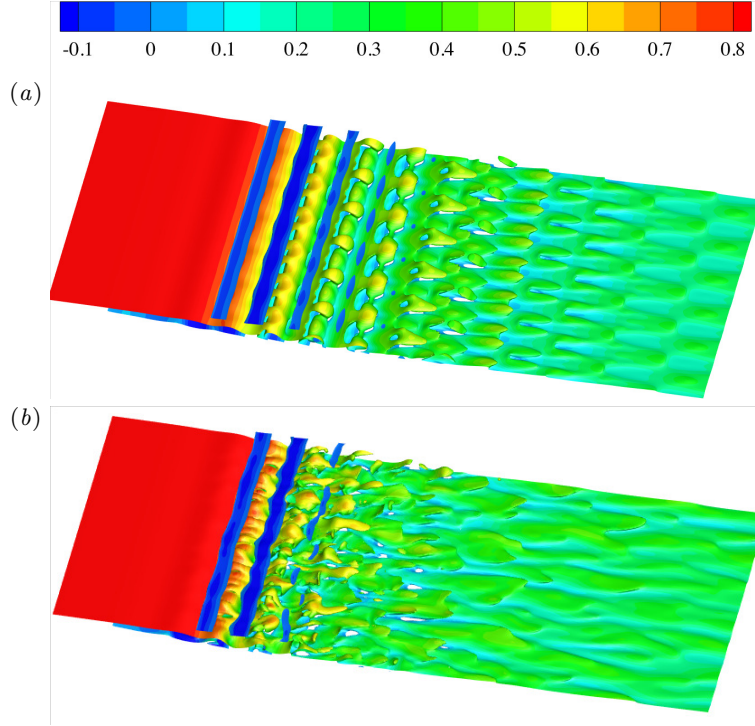
FIGURE 10. Iso-surfaces of spanwise vorticity -0.7 (coloured by streamline velocity) in the flow perturbed by the optimal inflow perturbation at $\beta = 0$, $\omega = 0.5$, $\tau = 150$ and (*a*) $s = 0.01$, and (*b*) $s = 0.02$.

less than 0.3% of the inflow velocity in the base flow, vortex shedding occurs downstream of the bubbles where the perturbations are mostly amplified while the separation and reattachment of the two bubbles are almost intact. At $s = 0.001$, the oscillation, or flapping of the reattachment point of the secondary bubble is observed. At $s = 0.005$, the flapping extends to the reattachment point of the primary bubble and the separation point of the secondary bubble. It is worth noting that for the $s = 0.001$ and 0.005 cases, the vortex shedding does not maximise at $x = 28$ as revealed in the linear simulations, owing to the nonlinear interaction of the perturbations, which limits the linearly predicted amplifications.

The three-dimensional perturbed flow at $s = 0.01$ and $s = 0.02$ is shown in Fig. 10. It is seen that at $s = 0.01$, six periods can be identified in the spanwise direction, corresponding to dominant wavenumber $\beta = 1.8$. This wavenumber is much higher than the reported wavenumbers of the most unstable three-dimensional waves ($\beta = 0.91$ in Barkley *et al.* (2002)) and the optimal initial perturbations ($\beta = 0.645$ in Blackburn *et al.* (2008)), since this three-dimensionality is developed based on a two-dimensional vortex-shedding flow, instead of an unperturbed steady flow, where the reported most energetic three-dimensional modes are calculated. For $s = 0.02$, the flow becomes more turbulent and no dominant wavenumbers can be identified. As s increases, the secondary bubble moves upstream and its spanwise oscillation can be clearly observed at $s = 0.02$.

The flapping of the bubbles, or the oscillation of the separation and reattachment points, can be more quantitatively studied by calculating the point on the wall where the shear stress changes sign. For three-dimensional flow, the shear stress is averaged across the spanwise direction. The time development of the separation and reattachment
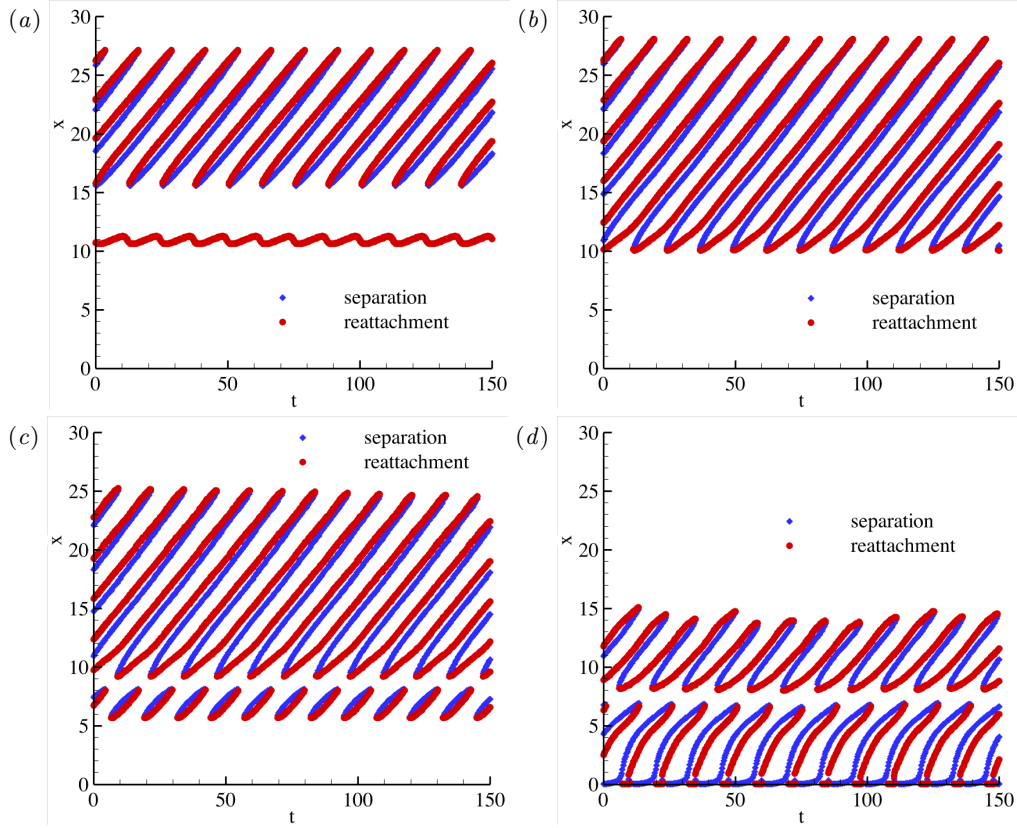
FIGURE 11. Oscillation of separation and reattachment points on the lower wall when the flow is perturbed by the optimal inflow perturbation at $\beta = 0$, $\omega = 0.5$ and $\tau = 150$. The magnitude of the inflow perturbation is $s = 0.001, 0.005, 0.01$ and 0.02 for (a), (b), (c) and (d) respectively.

points is revealed in Fig. 11. The perturbed flow has been evolved 150 time units to wash out the transient effects before collecting the separation/reattachment points for another 150 time units. To focus on the flapping of the primary bubble, only the lower wall is considered.

At $s = 0.001$, the reattachment point of the primary bubble oscillates with a small magnitude, while three or four smaller bubbles can be observed at a given time, as shown in Fig. 11(a). These smaller bubbles are associated with the string of wall vortices induced by the main vortices (see Fig. 8) downstream of the primary bubble. As discussed above, the nonlinear interaction of the perturbations limits the vortex shedding downstream of the bubbles and therefore these smaller bubbles shrink and finally vanish around $x = 28$. Both the primary bubble and the smaller bubbles oscillate with the frequency of the inflow perturbation, i.e. $\omega = 0.5$, corresponding to Strouhal number St $= 0.08$. The Strouhal number of bubble flapping in flow past a backward-facing step has been observed to be 0.06 (Le *et al.* 1997), 0.07 (Métais 2001) and $O(0.1)$ (Wee *et al.* 2004) in fully turbulent regimes. This close match of the Strouhal number between the current and previous works indicates that the flapping can be a result of receptivity to the energetic inflow noise.

At $s = 0.005$, the small bubbles become stronger and move upstream until the reattachment point of the primary bubble, as can be seen in Fig. 11(b). The reattachment curves
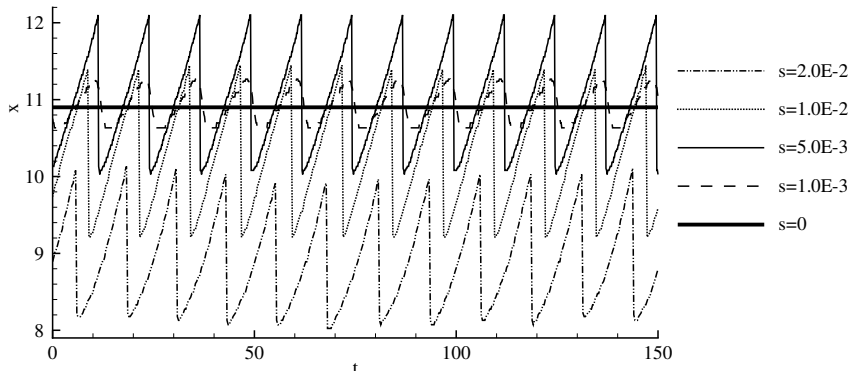
FIGURE 12. Flapping of the reattachment point of the primary bubble at $\beta = 0$, $\omega = 0.5$ and $\tau = 150$.

consists of two connected segments, one with lower slope at $10 < x < 13$, corresponding to the primary bubble and the other with higher slope at $13 < x < 28$, corresponding to the smaller bubbles. Owing to the upstream extension of the smaller bubbles compared with the $s = 0.001$ case, four or five smaller bubbles can be identified at a given time.

At $s = 0.01$, where the maximum inflow velocity perturbation reaches 0.014 (non-dimensionalized by the maximum inflow velocity of the unperturbed flow), another string of bubbles appear inside the primary bubble and vanish before reaching the primary reattachment point as shown in Fig. 11(c). The smaller bubbles downstream of the primary bubble vanish at around $x = 25$, owing to the nonlinear interaction of perturbations, which enhances mixing and prevents the generation of separation bubbles. At a given time, four or five smaller bubbles can be identified, with one upstream and others downstream of the primary reattachment point.

At $s = 0.02$, where the maximum inflow perturbation reaches 0.028 (2.8% of the maximum inflow velocity of the unperturbed flow), the flow becomes turbulent, which further prevents separation. Therefore as can be seen in Fig. 11(d), only one or two smaller bubble can be identified downstream of the primary reattachment point and it vanishes around $x = 15$. However, two smaller bubbles appear inside the primary bubble and extend upstream until the step. For all the s studied, the bubble flapping frequency is associated with the frequency of the inflow perturbations.

The flapping of the reattachment point of the primary bubble is extracted from Fig. 11 by taking the shortest distance in the range $8 < x < 28$ (to exclude the smaller bubbles inside the primary bubble) into consideration (Schäfer *et al.* 2009). As shown in Fig. 12, the unperturbed ($s = 0$) reattachment is steady. At small values of s, e.g. $s = 0.001$ or 0.005, the reattachment point oscillates periodically around the unperturbed point, while the magnitude of the oscillation increases with s. When the flow becomes three-dimensional at $s = 0.01$, the enhanced mixing reduces the size of the primary bubble. At $s = 0.02$, the flow is turbulent and the size of the primary bubble reduces further but is still flapping significantly. The flapping frequency of the primary bubble is not clearly altered by the nonlinear developments and even in three-dimensional and turbulent conditions, the flapping frequency is still associated with that of the inflow perturbation.

4.4. *Nonlinear development of random inflow noise*

In physical experiments, the inflow boundary condition is perturbed by random noise. Using notations introduced in Appendix A, a random inflow noise can be decomposed as a
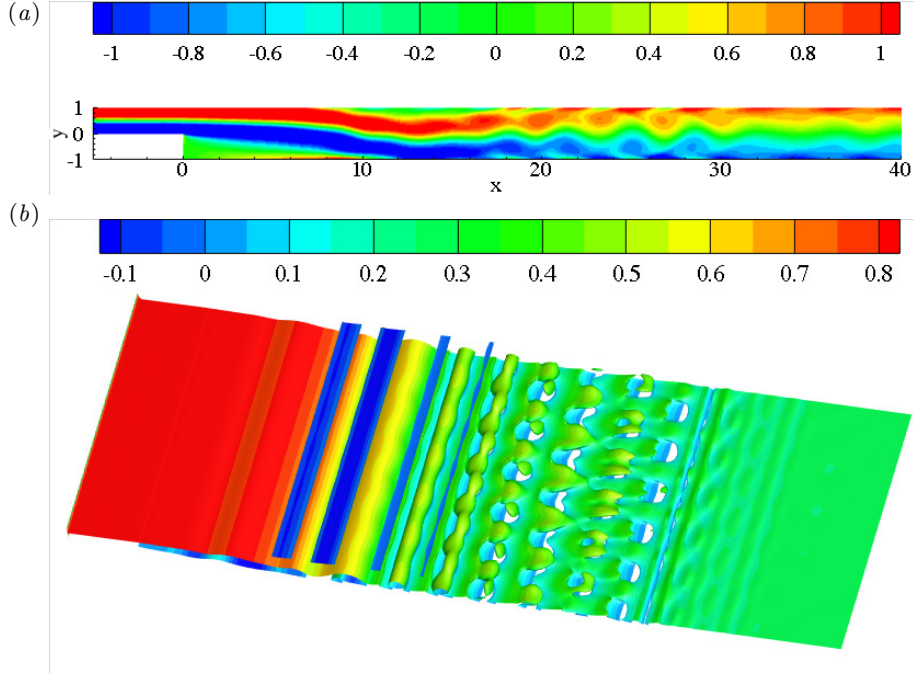
FIGURE 13. Outcome of the random inflow perturbation at $\beta = 0$, $\omega = 0.5$ and $\tau = 150$. (a) Contours of spanwise vorticity of the two-dimensional outcome at inflow turbulent intensity 0.01; (b) iso-surface of spanwise vorticity -0.7 (coloured by streamline velocity) in the three-dimensional outcome at inflow turbulent intensity 0.05.

linear combination of the eigenvectors of a joint operator $\mathcal{M}^*(\tau)\mathcal{M}(\tau)$. Since the optimal inflow perturbation is the leading eigenvector of this operator, it can be considered as a component of the random noise. Therefore the development of the optimal inflow perturbation is expected to be observed in the flow perturbed by random inflow noise. Kaiktsis *et al.* (1996) have used inflow noise with random spatial distributions but a prescribed frequency to perturb the backward-facing step flow and observed that the flow response reaches maximum to inflow noise with Strouhal number $0.05 \sim 0.104$. In this subsection, the spatially and temporally random inflow noise is adopted to explore the footprint of the optimal boundary perturbation in a real flow.

The randomly perturbed flow at two typical values of the inflow turbulent intensity, i.e. 0.01, where vortex shedding is clearly observed, and 0.05, where the flow becomes three-dimensional, is shown in Fig. 13. It is seen that the vortex shedding downstream of the secondary bubble observed in the optimally perturbed flow in Fig. 9 is also present in the randomly perturbed flow. However, since only a fraction of the random inflow noise is in the form of the optimal inflow perturbation, the random noise perturbs the flow and activates vortex shedding much less efficient than the optimal perturbations. In the three-dimensional flow induced by random inflow noise illustrated in Fig 13(b), 6 periods can be identified in the spanwise direction, similarly as observed in the optimally perturbed case (see Fig 10a).

To further illustrate the role of optimal inflow perturbations in the randomly perturbed flow, the oscillation of separation and reattachment points on the lower wall owing to the random noise is plotted in Fig. 14. It is observed that there are around 12 periods for the small bubbles downstream of the main bubble contained over time interval 150, similarly
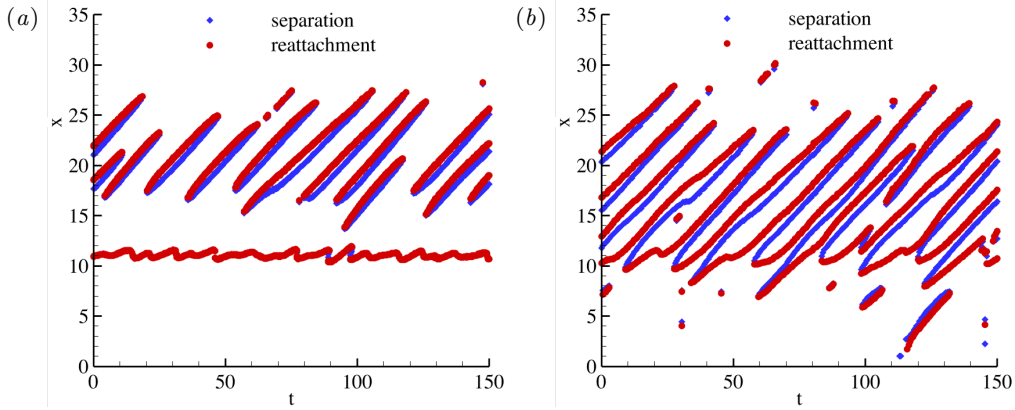
FIGURE 14. Oscillation of separation and reattachment points on the lower wall when the flow is perturbed by the random inflow perturbation at turbulent intensity (*a*) 0.01 and (*b*) 0.05.
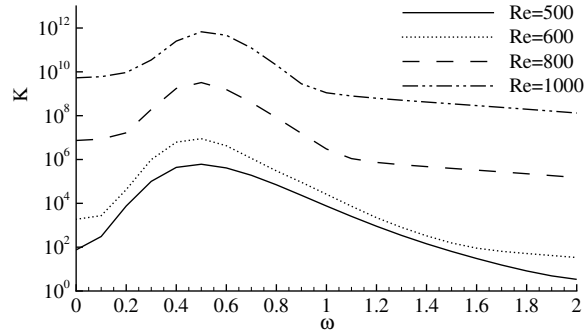

FIGURE 15. The Reynolds number dependence of the gain to optimal inflow noise at $\tau = 150$ and $\beta = 0$.

as can be seen in Fig. 11. This observation indicates that the bubbles oscillate with frequency around $\omega = 0.5$, at which the receptivity maximises, and therefore manifests amplifications of the optimal inflow perturbations in this randomly perturbed flow.

4.5. *Receptivity at higher Reynolds number*

In this subsection, the Reynolds number dependence of the receptivity to inflow noise is studied. Since the recirculation bubble in the base flow extends downstream at higher Reynolds number and the perturbation is expected to reach maximum at further down-stream locations, the outflow section is extended to 100 in this subsection. The spanwise wavenumber and final time are fixed at $\beta = 0$ and $\tau = 150$ respectively.

From Fig. 15, it is noticed that the gain increases dramatically as the Reynolds number is increased from 500 to 1000, while the maximum appears at $\omega = 0.5$ over all the cases considered. The linear outcomes of the optimal inflow perturbations at different Reynolds number are presented in Fig. 16, where the border of the recirculation bubbles in the base flow are plotted together. It is seen that at higher Reynolds number, the upper bubble extends downstream, inducing a longer "grow" section associated with the inflectional point instability, and the rectangular structure appears further downstream. These observations suggest that the mechanism of noise amplifications at higher Reynolds number considered here is similar as that discussed in § 4.2, where the Reynolds number is fixed at 500.
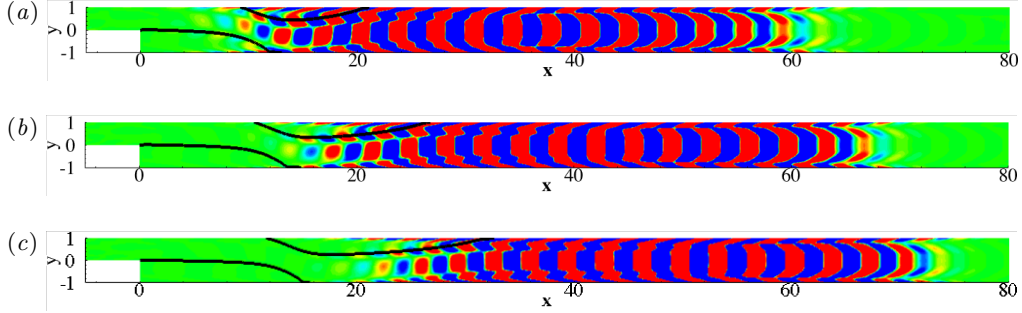
FIGURE 16. Contours of spanwise vorticity of the outcome of the optimal inflow boundary perturbation at $\beta = 0$, $\tau = t = 150$, $\omega = 0.5$ and (a) $Re = 600$, (b) $Re = 800$ and (c) $Re = 1000$. Different contour levels are chosen in each plot to highlight structures. Thick solid lines represent the borders of recirculation bubbles.
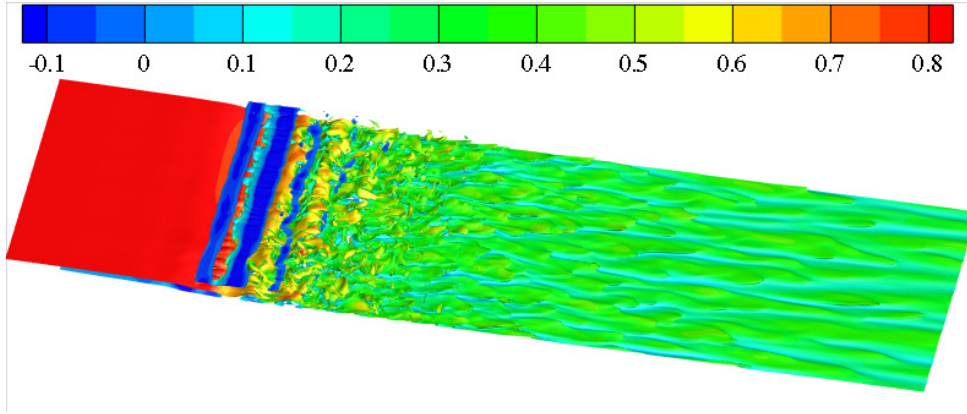

FIGURE 17. Iso-surfaces of spanwise vorticity -0.7 (coloured by streamline velocity) in the flow perturbed by the optimal inflow perturbation at $\beta = 0$, $\omega = 0.5$, $\tau = 150$, $s = 0.001$ and $Re = 1000$.

The nonlinear evolution of the optimal perturbation is further investigated by DNS of the base flow perturbed by the inflow noise at $Re = 1000$, $\beta = 0$, $\tau = 150$ and $\omega = 0.5$. Owing to the large magnitude of noise amplifications as shown in Fig. 15, even at perturbation magnitude $s = 0.001$, the flow develops into a three-dimensional and turbulent pattern before reaching the end of the upper bubble. This observation confirms that the flow at $Re = 1000$ is much more sensitive to inflow noise than that at $Re = 500$ and indicates that the "growth" section is not fully exploited at this magnitude of inflow noise.

5. Base flow modification on receptivity to inflow noise

To further illustrate the mechanism of receptivity to inflow noise and explore the control of receptivity, an optimal body force is calculated to modify the base flow. As presented above in (2.12), the magnitude of the gradient of the Lagrangian functional with respect to the body force, measured as the square integration across the domain, $(\nabla_f \mathcal{L}, \nabla_f \mathcal{L})$, evaluates the effectiveness of the optimal body force in modifying the base flow and its receptivity. It is seen in Fig. 18 that the magnitude of this gradient maximises
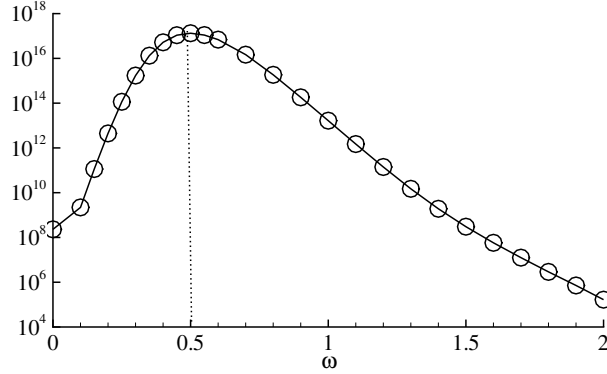
FIGURE 18. Square integration of the gradient of the Lagrangian with respect to the body force, i.e. $(\nabla_f \mathcal{L}, \nabla_f \mathcal{L})$, at $\tau = 150$ and $\beta = 0$.
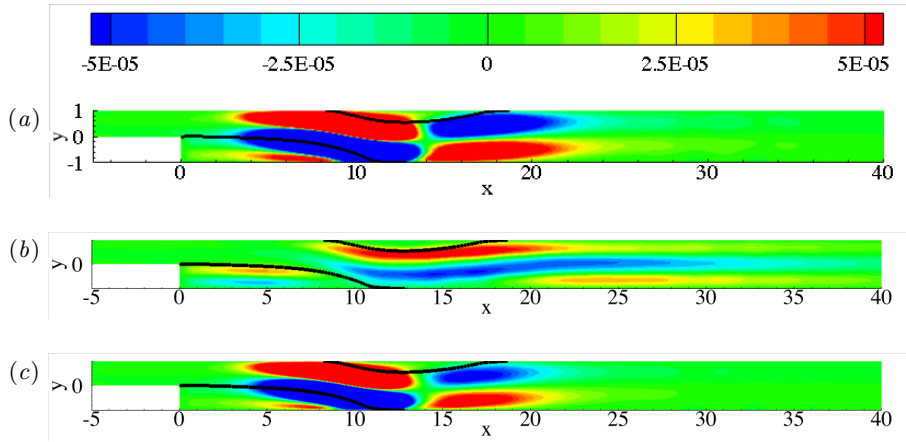

FIGURE 19. Contours of the streamwise velocity of the base flow modification (difference between the forced and unforced base flow), with $r = -10^{-5}$. The body force is obtained at $\tau = 150$, $\beta = 0$ and (a) $\omega = 0$, (b) $\omega = 0.5$ and (c) $\omega = 1.5$. Thick solid lines denote the border of unforced recirculation bubbles.

at $\omega = 0.50$, indicating that the strongest receptivity, which also occurs at $\omega = 0.50$, is most tenable to be controlled by the body force.

Owing to the linearisation of the governing equations, the body force calculated in (2.12) optimally modifies the base flow and its receptivity only when the body force is small enough. In Fig. 19, a scale factor $r = -10^{-5}$, which is in the linear regime as will be shown in Fig. 20, is adopted to illustrate the modification of the base flow owing to the optimal body force. This negative scale factor is expected to reduce the receptivity of the base flow to inflow noise. At $\omega = 0$ and $\omega = 1.5$ the change of the base flow is concentrated around the fore segment of the secondary bubble and the rear part of the primary bubble, both of which tend to suppress the bubble instabilities and consequently the receptivity. At $\omega = 0.5$, the modification is extended downstream of the bubbles and tends to flatten the vertical distribution of the base flow velocity (reducing $|dU/dy|$), decelerate the generation of left-headed perturbation streamlines and subsequently reduce the perturbation growth. Physically these base flow modifications can be achieved by, e.g., boundary blowing around the separation point of the secondary bubble along the border streamline of the bubble, which injects momentum into the separating flow, and
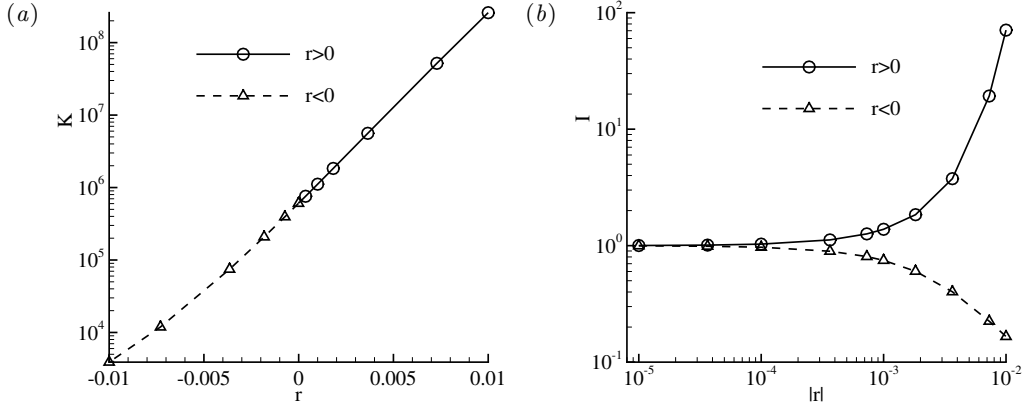
FIGURE 20. (*a*) The gain K for forced base flow and (*b*) indicator of the linear dynamics I at $\omega = 0.5$, $\tau = 150$ and $\beta = 0$.
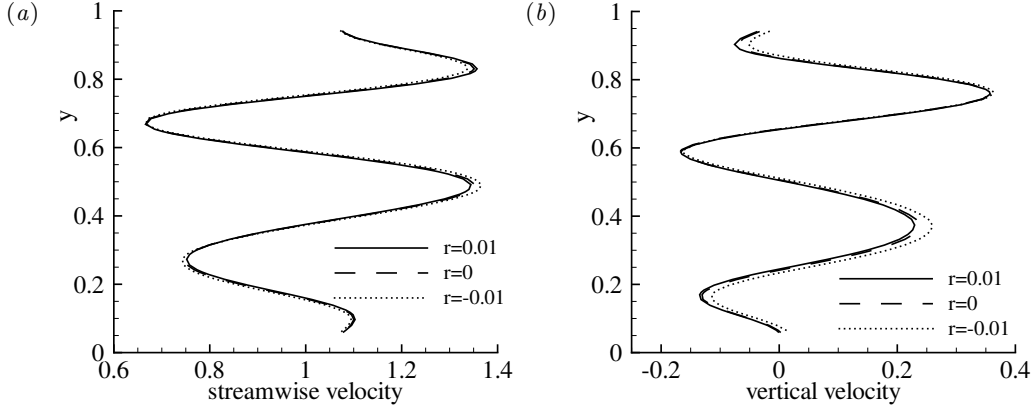

FIGURE 21. Comparison of the optimal inflow perturbations $\tilde{\boldsymbol{u}}_b$ to the forced and unforced base flow at $\tau = 150$, $\omega = 0.5$ and $\beta = 0$. (*a*) Streamwise velocity component and (*b*) vertical velocity component. The magnitude is normalised to be $[\tilde{\boldsymbol{u}}_b, \tilde{\boldsymbol{u}}_b] = 1$.

blowing around the reattachment line of the primary bubble in the direction along the border streamline of the bubble.

The receptivity of the optimally modified base flow is shown in Fig. 20(*a*). Over the range of r considered, i.e. $-0.01 \leq r \leq 0.01$, a steady solution of the base flow has been obtained, indicating that the forced base flow is asymptotically stable at least to two-dimensional perturbations. It is noticed that as expected from (2.12) a positive scale factor r increases the gain K, while a negative r reduces the gain. To verify the linearly predicted effects of the body force on receptivity, define an indicator

$$I = \Delta K/(\nabla_{\boldsymbol{f}}\mathcal{L}, \boldsymbol{f}) = \Delta K/(\nabla_{\boldsymbol{f}}\mathcal{L}, r\nabla_{\boldsymbol{f}}\mathcal{L}),$$

where ΔK is the difference of the gain using forced and unforced base flow. If $|r|$ is small enough, the body force works in the linear range and the indicator I is expected to be 1. At the smallest levels of $|r|$ considered, i.e. $r = 10^{-5}$, $K = 1.0026$, and at increasing $|r|$, I deviates from 1 significantly as the nonlinear effects become non-negligible, as shown in Fig. 20(*b*). It is also noticed that $I < 1$ for negative r, owing to the restriction that the gain has to be positive and therefore ΔK has a lower bound.
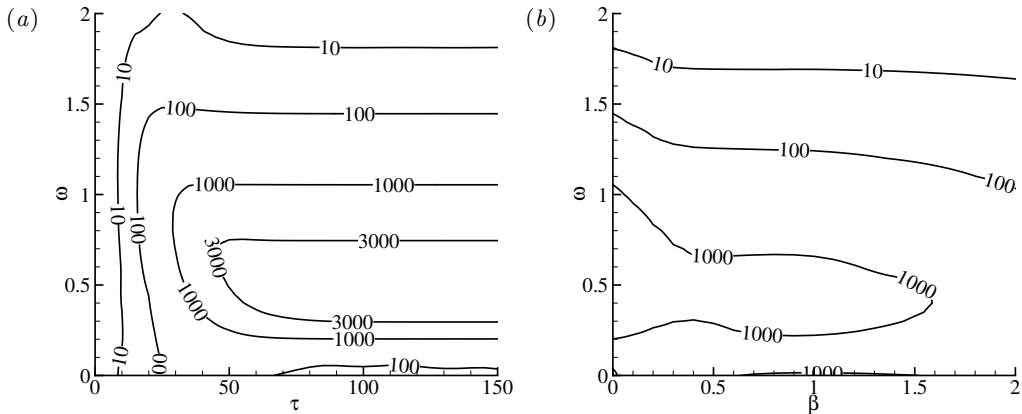
FIGURE 22. Contours of the gain K of the modified base flow at (a) $\beta = 0$ and (b) $\tau = 150$. The base flow modification is obtained at $\tau = 150$, $\beta = 0.5$, $\omega = 0$ and $r = -0.01$.

Effects of the base flow modification on the distributions of the optimal inflow perturbation is revealed in Fig. 21. It is seen that for the scale factors considered, the change of the optimal inflow perturbation is trivial, indicating that the body force acts to weaken/strengthen the existing mechanism of receptivity, but does not modify the base flow or the receptivity mechanism fundamentally. It is calculated that the relative change of the base flow, measured as $(\boldsymbol{U}(-0.01), \boldsymbol{U}(-0.01)/(\boldsymbol{U}(0), \boldsymbol{U}(0)))$, where the base flow is considered as a function of the scale factor r, is less than 0.05%.

The optimal base flow modification presented in Fig. 19 is calculated at $\tau = 150$, $\beta = 0$ and $\omega = 0.5$, and has the expected effects on receptivity at the "design" parameters as presented in Fig. 20. The control effects of this modification to receptivity at the out-of-design conditions are illustrated in Fig. 22. It is observed that the gain at out-of-design final time and spanwise wavenumbers is also suppressed at the negative scale factor $r = -0.01$. However, the receptivity at out-of-design frequencies is much less suppressed, since the optimal base flow modifications at these frequencies are dramatically different with that at $\omega = 0.5$, as has been discussed in Fig. 19. For the modified base flow, the maximum gain still appears at around $\omega = 0.5$, $\tau = 150$ and $\beta = 0$, confirming that the mechanism of receptivity is weakened but not fundamentally altered. It is also worth noting that the transient effects are significantly suppressed: the contour levels become more flatten with τ, suggesting that the long-term amplification to inflow noise and the transient energy growth are highly correlated.

6. Correlation between amplifications to initial and boundary perturbations

In this section, the correlation between receptivity to inflow noise and receptivity to initial perturbations is explored by comparing the body forces that optimally modify amplifications to initial and boundary perturbations. The receptivity to initial perturbations and the associated transient energy growth in flow past a backward-facing step have been well studied. The optimal initial perturbation and its outcome are reproduced in the current work for further studies of base flow modifications, as shown in Fig. 23. As presented in § 5, the receptivity to inflow noise maximises at $\beta = 0$ while the receptivity to initial perturbations was reported to maximise at $\beta = 0.645$ with a slight increment from that at $\beta = 0$ (Blackburn *et al.* 2008). Therefore to compare the mechanisms of
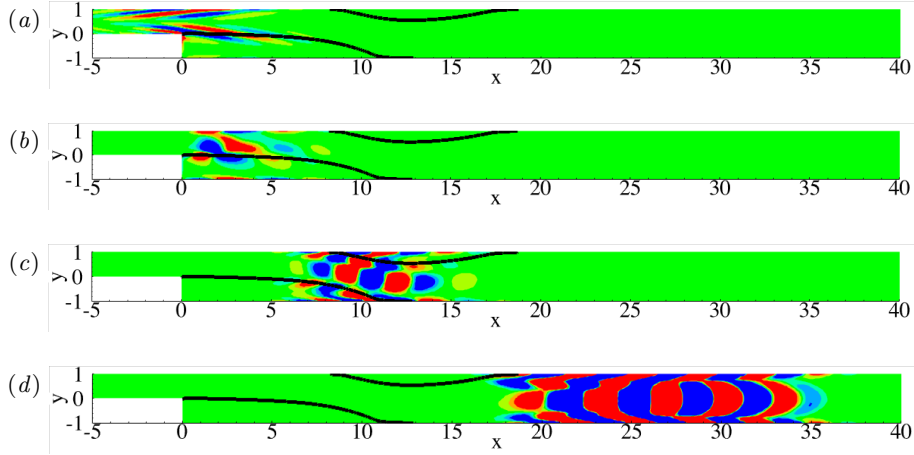
FIGURE 23. Contours of spanwise vorticity in the development of the optimal initial perturbation at $\tau = 58.1$, $\beta = 0$ and (a) $t = 0$, (b) $t = 4$, (c) $t = 20$ and (d) $t = 58.1$. Different contour levels are chosen in each plot to highlight structures. Thick solid lines denote the border of recirculation bubbles.

the amplification of inflow and initial perturbations, $\beta = 0$ is adopted in the initial perturbation calculations.

The final time at which the transient energy growth of the optimal initial perturbation reaches maximum is $\tau = 58.1$, agreeing well with that reported by Blackburn *et al.* (2008). It is seen that the optimal initial perturbation is located around the step and tilts backwards against the shear of the base flow from Fig. 23(a). When this initial perturbation is convected downstream, it is compressed and amplified by the Orr mechanism (Vanneste 1999; Guégan *et al.* 2006), as shown in Fig. 23(b). Further downstream, in the region around the bubbles, the inflectional point instability manifests itself as presented in Fig. 23(c). In the region downstream of the secondary bubble, the misalignment mechanism can be observed in Fig. 23(d): the perturbation consists of left-headed, rectangular and right-headed structures, with the rectangular profile appearing around $x = 28$, similarly as seen in Fig. 6(b). As mentioned before, the choice of contour levels in Fig. 23(d) presents clearer that the magnitude of the perturbation grows upstream of the rectangular structure and decays downstream of it, which validates the theoretical results derived from (4.4). Therefore receptivities to both inflow and initial noise rely on the bubble instabilities and the misalignment mechanism for perturbation amplifications. However, in receptivity to inflow noise, the perturbation cannot take advantage of the Orr mechanism, since the inflow noise would be convected by the base flow to decline forwards instead of backwards.

Following the procedure presented in § 2.5, the body force that optimally modify the base flow's amplification to initial perturbations can be calculated. To illustrate the relation between receptivities to initial and boundary perturbations, the correlation between the forces optimally modifying the amplifications to initial and boundary perturbations can be computed as

$$\rho = (\boldsymbol{f}_{bp}, \boldsymbol{f}_{ip})/\sqrt{(\boldsymbol{f}_{ip}, \boldsymbol{f}_{ip})(\boldsymbol{f}_{bp}, \boldsymbol{f}_{bp})} \tag{6.1}$$

where $\boldsymbol{f}_{bp}$ refers to the body force optimally modifying amplifications to boundary perturbations (inflow noise) at a large enough final time $\tau = 150$ so as to eliminate the transient energy growth, and $\boldsymbol{f}_{ip}$ is the body force that optimally modifying amplifica-
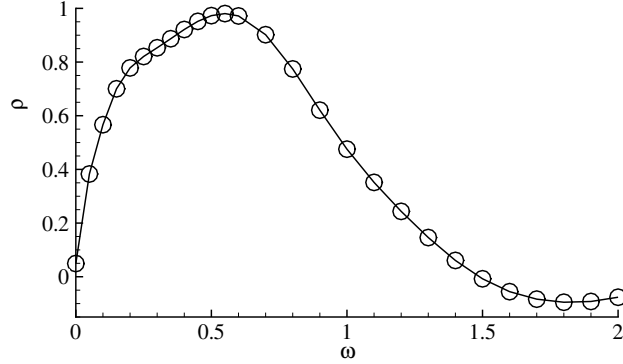
FIGURE 24. Correlation of the body forces that optimally modify the amplifications to inflow noise at $\beta = 0$, $\tau = 150$ and various frequencies and the initial perturbation at $\beta = 0$ and $\tau = 58.1$.
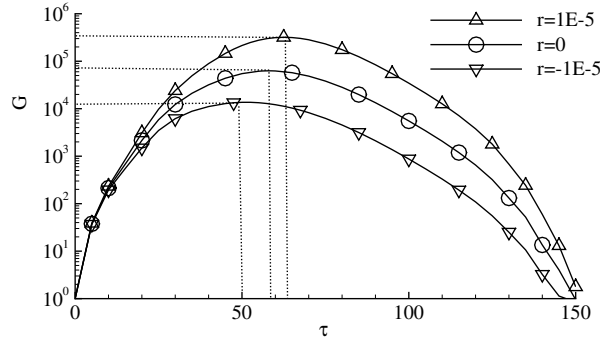

FIGURE 25. Transient growth of the controlled and uncontrolled flow at $\beta = 0$. The maximum growth point in each curve is highlighted by dotted lines.

tions to initial perturbations at $\tau = 58.1$, where the transient growth maximises over the parameters considered.

As revealed in Fig. 24, the correlation $\rho \approx 0$ at $\omega = 0$, indicating that the receptivities to steady inflow noise and the optimal initial perturbation are almost decoupled. At $\omega \approx 0.5$, where the receptivity to inflow noise reaches maximum, the correlation between receptivities to inflow and initial perturbations also maximises and reaches 0.973, indicating that the two body forces almost overlap. This observation suggests that the most dramatic amplifications to inflow perturbations and initial perturbations rely on the same mechanisms (the bubble instabilities and the misalignment mechanism) and can be controlled simultaneously by a body force. It is also noticed that as ω becomes larger, this correlation drops, in agreement with the previous discussion that the receptivity to inflow noise at high frequencies relies on the primary bubble instability and is almost irrelevant with the misalignment mechanism downstream of the secondary bubble.

It is worth mentioning that there is another more intuitive option to illustrate the correlation between receptivities to boundary and initial perturbations, i.e. comparing the outcomes of the optimal initial perturbation and the optimal inflow perturbation. However, as can be seen in Fig. 6(b), the outcome of the optimal boundary perturbation spreads over the region downstream of the step, while as shown in Fig. 23(d), the outcome of the optimal initial perturbation is located downstream of the bubbles and the contribution of the bubble instabilities to the energy growth is not directly revealed

owing to the convection effects. Therefore the profile of the perturbation outcome does not cover all the amplification mechanisms, and the correlation of the outcomes of the initial and boundary perturbations is physically less meaningful than the correlation of the optimal body forces.

The receptivity to initial perturbations, measured by the transient energy growth G, which is calculated using the unforced and optimally forced base flow, is shown in Fig. 25. It is seen that at scale factor $|r| = 10^{-5}$, the maximum transient growth can be enhanced or suppressed by an order. As the transient growth is suppressed (enhanced), the optimal final time reduces (increases), since in the modified flow, the rectangular streamlines appear earlier (later), further confirming the misalignment mechanism in noise amplifications.

7. Conclusion

The noise amplification of the flow past a backward-facing step with an expansion ratio 0.5 is investigated. As has been adopted in a previous work (Blackburn *et al.* 2008), in most of this work, the Reynolds number is fixed at $Re = 500$, at which the unperturbed base flow is steady and two-dimensional, featuring a primary bubble and a secondary bubble attached to the lower wall and upper wall respectively. According to the source of the perturbations, the amplification effect can be classified as receptivity to initial perturbations and receptivity to inflow boundary perturbations.

Since the receptivity to initial perturbations (transient growth of the initial perturbation) in flow past a backward-facing step has been well studied, this work focuses on the receptivity to inflow noise. A large enough final time $\tau = 150$ is adopted so as to isolate the receptivity from transient energy growth. It is found that the receptivity to inflow noise maximises at spanwise wavenumber $\beta = 0$ and frequency $\omega = 0.5$, at which the magnitude of the inflow velocity perturbation is amplified over two orders. The receptivity can be explained as a combination of the bubble induced inflectional point instabilities and a misalignment mechanism, which transfers perturbations downstream of the secondary bubble to left-headed, rectangular and right-headed structures. The magnitude of the perturbation grows in the left-headed region until reaching the rectangular profile, downstream of which in the right-headed region, the magnitude decays. In the further downstream region, the base flow stretches the perturbation and the structure becomes sharper right-headed. Therefore the perturbation growth induced by the misalignment mechanism is self-limited. The most amplified inflow perturbation, i.e. with $\omega = 0.5$, takes full advantage of the bubble instabilities and misalignment mechanisms, while perturbations with higher or lower frequencies are only amplified around the primary bubble and the fore segment of the secondary bubble. Similar optimal frequency and receptivity mechanisms are observed at higher Reynolds number up to $Re = 1000$.

The nonlinear development of the optimal boundary perturbation is studied through DNS. It is observed that at low magnitudes of inflow perturbations, vortex shedding appears downstream of the secondary bubble. As the magnitude of perturbations increases, flapping of the separation and reattachment points of the bubbles is observed and smaller bubbles are induced along the wall. As the maximum inflow perturbation reaches 1.4% of the free stream velocity, the flow becomes three-dimensional. It is also observed that the three-dimensional and turbulent developments of the perturbed flow enhance mixing and significantly reduce the size of the recirculation zones. The Strouhal number of bubble flapping in the flow perturbed by both the optimal and random inflow noise is 0.08, which agrees with the frequency of the globally optimal inflow perturbation. This Strouhal number has been reported to be 0.06 (Le *et al.* 1997), 0.07 (Métais 2001),

$0.05 \sim 0.1$ (Kaiktsis *et al.* 1996) and $O(0.1)$ (Wee *et al.* 2004) at larger Reynolds number or in fully turbulent regimes. Even though these previous results are obtained at larger Reynolds number, the close agreement with the current work suggests that the bubble flapping can be a subsequence of receptivity to inflow noise.

Base flow modifications are further conducted to reveal the mechanism of noise amplifications and explore the control of receptivities. To reserve the divergence free condition, the base flow is modified by a body force. It is worth noting that a boundary suction/blowing can be physically more useful to modify or control the base flow, but the body force is more effective to change the flow even in the region far from boundaries and therefore a suitable tool to study the mechanism of noise amplifications. A numerical methodology is established to calculate the linearly optimal body force and this methodology accommodates both initial and boundary perturbation problems. The distribution of the base flow modification owing to the linearly optimal body force is found to be strongly correlated with the outcome of the inflow noise. At $\omega = 0.5$, the modification is located around the bubbles and the shear layers downstream of the bubble, which modifies the bubble induced instabilities and the misalignment mechanism. At lower and higher frequencies, the modification concentrates around the primary bubble and the fore part of the secondary bubble, reflecting the irrelevance of the misalignment mechanism in the region downstream of the secondary bubble in these cases. However, the distribution of the optimal inflow perturbation is insensitive to the base flow modifications, indicating that the modification does not alter the fundamental feature of the flow. A modification with relative energy change 0.05% is found to reduce the maximum receptivity by around two orders. The modification effects on receptivity are reserved at out-of-design final time and spanwise wavenumbers, but do not work well for out-of-design noise frequencies, owing to variation of mechanisms at difference frequencies.

In optimal initial perturbation studies, it is confirmed that the transient energy growth of the initial perturbation also stems from the bubble instability and the misalignment mechanism. From the correlation of the body forces that optimally modify receptivities to inflow and initial perturbations, it is found that the base flow modification that suppresses receptivity to initial perturbations also suppresses receptivity to inflow perturbations at the most amplified frequency. However, at higher or lower frequencies, the correlation drops, confirming that the high and low frequency receptivity to inflow noise relies on different mechanisms with the transient energy growth of initial perturbations. The base flow modification study also suggests that the optimal body force or the optimal modification reveals the complete mechanisms of noise amplifications, which cannot be fully identified from the outcome of the optimal initial or boundary perturbations.

Appendix A. Lagrangian functional

Similarly as presented in (2.7), a "symmetric" Lagrangian functional can be defined

$$
\begin{aligned}
\mathcal{L} = K &+ \langle \boldsymbol{\lambda}_1, \partial_t \boldsymbol{u} - L(\boldsymbol{U})\boldsymbol{u} \rangle + \langle \boldsymbol{\lambda}_2, \partial_t \boldsymbol{u}^* + L^*(\boldsymbol{U})\boldsymbol{u}^* \rangle \\
&+ [\boldsymbol{\lambda}_3, \boldsymbol{g}(\boldsymbol{u}^*) - K\tilde{\boldsymbol{u}}_b] + (\boldsymbol{\lambda}_4, \boldsymbol{u}(\tau) - \boldsymbol{u}^*(\tau)) + (\boldsymbol{\lambda}_5, D\boldsymbol{U} - \boldsymbol{f}), \quad \text{(A 1)}
\end{aligned}
$$

where $\boldsymbol{\lambda}_i$ ($1 \leq i \leq 5$) are Lagrangian multipliers: $\boldsymbol{\lambda}_1$ and $\boldsymbol{\lambda}_2$ are time-dependent variables defined on the domain Ω and time interval $[0, \tau]$, $\boldsymbol{\lambda}_3$ is a time-independent variable defined on the perturbation boundary $\partial\Omega_b$ and $\boldsymbol{\lambda}_4$ and $\boldsymbol{\lambda}_5$ are time-independent variables on Ω. The first term on the right-side is the optimal gain over all possible boundary perturbations, the second, third, fourth and fifth terms are the constraint that $\tilde{\boldsymbol{u}}_b$ is the optimal boundary perturbation, and the final term is the constraint that the base flow $\boldsymbol{U}$ is a steady solution of the forced NS equations (2.1).

One may integrate the second and third terms in the definition of the Lagrangian functional (A 1) by parts to obtain

$$\mathcal{L} = K - \langle \boldsymbol{u}, \partial_t \boldsymbol{\lambda}_1 + L^*(\boldsymbol{U})\boldsymbol{\lambda}_1 \rangle + (\boldsymbol{u}(\tau), \boldsymbol{\lambda}_1(\tau)) - [\boldsymbol{g}(\boldsymbol{\lambda}_1), \tilde{\boldsymbol{u}}_b] - \langle \boldsymbol{u}^*, \partial_t \boldsymbol{\lambda}_2 - L(\boldsymbol{U})\boldsymbol{\lambda}_2 \rangle$$
$$+ (\boldsymbol{u}^*(\tau), \boldsymbol{\lambda}_2(\tau)) - [\boldsymbol{g}(\boldsymbol{u}^*), \boldsymbol{\lambda}_{2b}] + [\boldsymbol{\lambda}_3, \boldsymbol{g}(\boldsymbol{u}^*) - K\tilde{\boldsymbol{u}}_b] + (\boldsymbol{\lambda}_4, \boldsymbol{u}(\tau) - \boldsymbol{u}^*(\tau)) + (\boldsymbol{\lambda}_5, D\boldsymbol{U} - \boldsymbol{f}),$$
$$\text{(A 2)}$$

where $\boldsymbol{\lambda}_{2b}$ is defined on the perturbation boundary and satisfies $\boldsymbol{\lambda}_2(\tau) = \mathcal{M}(\tau)\boldsymbol{\lambda}_{2b}$, where $\mathcal{M}(\tau)$ is an operator evolving a boundary perturbation to a final outcome, whose action corresponds to the integration of the linearised NS equations.

Setting to zero the first variations of $\mathcal{L}$ with respect to $\boldsymbol{\lambda}_i$ ($1 \leq i \leq 5$) recovers the constraints that $\tilde{\boldsymbol{u}}_b$ is the optimal boundary perturbation leading to the largest gain K to the base flow $\boldsymbol{U}$ which is a steady solution of the NS equations (2.1). Setting the first variation of $\mathcal{L}$ to $\boldsymbol{u}^*(\tau)$, $\boldsymbol{u}(\tau)$, $\tilde{\boldsymbol{u}}_b$, $\boldsymbol{g}(\boldsymbol{u}^*)$ and K to zero, the following equations can be obtained,

$$\frac{\delta\mathcal{L}}{\delta\boldsymbol{u}^*(\tau)} = 0 \quad \Rightarrow \quad \boldsymbol{\lambda}_2(\tau) = \boldsymbol{\lambda}_4,$$

$$\frac{\delta\mathcal{L}}{\delta\boldsymbol{u}(\tau)} = 0 \quad \Rightarrow \quad \boldsymbol{\lambda}_1(\tau) = -\boldsymbol{\lambda}_4,$$

$$\frac{\delta\mathcal{L}}{\delta\tilde{\boldsymbol{u}}_b} = 0 \quad \Rightarrow \quad -\boldsymbol{g}(\boldsymbol{\lambda}_1) = K\boldsymbol{\lambda}_3$$

$$\frac{\delta\mathcal{L}}{\delta\boldsymbol{g}(\boldsymbol{u}^*)} = 0 \quad \Rightarrow \quad \boldsymbol{\lambda}_{2b} = \boldsymbol{\lambda}_3$$

$$\frac{\delta\mathcal{L}}{\delta K} = 0 \quad \Rightarrow \quad [\boldsymbol{\lambda}_3, \tilde{\boldsymbol{u}}_b] = 1,$$

from which eliminating $\boldsymbol{\lambda}_3$ and $\boldsymbol{\lambda}_4$, there are

$$[\boldsymbol{\lambda}_{2b}, \tilde{\boldsymbol{u}}_b] = 1, \qquad -\boldsymbol{g}(\boldsymbol{\lambda}_1) = K\boldsymbol{\lambda}_{2b} \qquad \text{and} \qquad \boldsymbol{\lambda}_1(\tau) = -\boldsymbol{\lambda}_2(\tau) \qquad \text{(A 3)}$$

Substituting operator $\mathcal{M}$ and its adjoint operator $\mathcal{M}^*$ whose action corresponds to the integration of the adjoint equation into (A 3) to reach

$$\mathcal{M}^*(\tau)\mathcal{M}(\tau)\boldsymbol{\lambda}_{2b} = K\boldsymbol{\lambda}_{2b}. \qquad \text{(A 4)}$$

Clearly $\boldsymbol{\lambda}_{2b}$ is the eigenvector of the joint operator $\mathcal{M}^*(\tau)\mathcal{M}(\tau)$ corresponding to the largest eigenvalue K. Therefore $\boldsymbol{\lambda}_{2b}$ is parallel with $\tilde{\boldsymbol{u}}_b$. Through standard algebraic manipulations, there are

$$\boldsymbol{\lambda}_{2b} = \tilde{\boldsymbol{u}}_b/[\tilde{\boldsymbol{u}}_b, \tilde{\boldsymbol{u}}_b], \quad \boldsymbol{\lambda}_2(\tau) = \boldsymbol{u}(\tau)/[\tilde{\boldsymbol{u}}_b, \tilde{\boldsymbol{u}}_b] \quad \text{and} \quad \boldsymbol{\lambda}_1(\tau) = -\boldsymbol{u}^*(\tau)/[\tilde{\boldsymbol{u}}_b, \tilde{\boldsymbol{u}}_b], \quad \text{(A 5)}$$

and therefore

$$\boldsymbol{\lambda}_1 = -\boldsymbol{u}^*/[\tilde{\boldsymbol{u}}_b, \tilde{\boldsymbol{u}}_b] \qquad \text{and} \qquad \boldsymbol{\lambda}_2 = \boldsymbol{u}/[\tilde{\boldsymbol{u}}_b, \tilde{\boldsymbol{u}}_b]. \qquad \text{(A 6)}$$

In (A 1), the variation of the second and third terms on the right-side with respect to

the base flow $\boldsymbol{U}$ can be formulated as

$$\delta\langle\boldsymbol{\lambda}_1, \partial_t\boldsymbol{u} - L(\boldsymbol{U})\boldsymbol{u}\rangle + \delta\langle\boldsymbol{\lambda}_2, \partial_t\boldsymbol{u}^* + L^*(\boldsymbol{U})\boldsymbol{u}^*\rangle =$$
$$\langle\delta\boldsymbol{U}, \nabla\boldsymbol{u}\cdot\boldsymbol{\lambda}_1\rangle - \langle\delta\boldsymbol{U}, \boldsymbol{u}\cdot\nabla\boldsymbol{\lambda}_1\rangle + \langle\delta\boldsymbol{U}, \nabla\boldsymbol{u}^*\cdot\boldsymbol{\lambda}_2\rangle + \langle\delta\boldsymbol{U}, \boldsymbol{\lambda}_2\cdot\nabla\boldsymbol{u}^*\rangle. \quad (A\,7)$$

In the derivation of this equation, (A 6) has been considered to eliminate the terms about surface integrations over the outflow boundary. Similarly the variation of the last term with respect to the base flow $\boldsymbol{U}$ can be written as

$$\delta(\boldsymbol{\lambda}_5, D\boldsymbol{U} - \boldsymbol{f})(\delta\boldsymbol{U}) = -(\delta\boldsymbol{U}, (L^*(\boldsymbol{U})\boldsymbol{\lambda}_5). \quad (A\,8)$$

Combining equations (A 7) and (A 8), the variation of the Lagrangian functional with respect to the base flow can be obtained,

$$\delta\mathcal{L}(\delta\boldsymbol{U}) = (\delta\boldsymbol{U}, \boldsymbol{F}_s - L^*(\boldsymbol{U})\boldsymbol{\lambda}_5), \quad (A\,9)$$

where

$$\boldsymbol{F}_s = \tau^{-1}\int_0^\tau (\nabla\boldsymbol{u}\cdot\boldsymbol{\lambda}_1 - \boldsymbol{u}\cdot\nabla\boldsymbol{\lambda}_1 + \nabla\boldsymbol{u}^*\cdot\boldsymbol{\lambda}_2 + \boldsymbol{\lambda}_2\cdot\nabla\boldsymbol{u}^*)\mathrm{d}t \quad (A\,10)$$

denotes the gradient of the Lagrangian functional with respect to the base flow, without the constraint that the base flow satisfies the NS equations (last term in (A 1)). Substituting (A 6) into (A 10) to reach

$$\boldsymbol{F}_s = \tau^{-1}\int_0^\tau (-\nabla\boldsymbol{u}\cdot\boldsymbol{u}^* + 2\boldsymbol{u}\cdot\nabla\boldsymbol{u}^* + \nabla\boldsymbol{u}^*\cdot\boldsymbol{u})\mathrm{d}t/[\tilde{\boldsymbol{u}}_b, \tilde{\boldsymbol{u}}_b]. \quad (A\,11)$$

Owing to the form of the Lagrangian functional, no further assumptions are introduced in the derivation of (A 11). Therefore the assumption that the base flow variation is zero on the boundaries as used in (2.14) can be released. Replacing $\boldsymbol{F}$ in (2.15) by $\boldsymbol{F}_s$ and following the procedures in § 2.5, the same results of the linearly optimal body force can be obtained.

REFERENCES

ARMALY, B., F. DURST, J. PEREIRA & SCHÖNUNG, B. 1983 Experimental and theoretical investigation of backward-facing step flow. *J. Fluid Mech.* **127**, 473–496.

BARKLEY, D., BLACKBURN, H. M. & SHERWIN, S. J. 2008 Direct optimal growth analysis for timesteppers. *Int. J. Num. Meth. Fluids* **57**, 1435–1458.

BARKLEY, D., GOMES, M. G. M. & HENDERSON, R. D. 2002 Three-dimensional instability in flow over a backward-facing step. *J. Fluid Mech.* **473**, 167–190.

BLACKBURN, H. M., BARKLEY, D. & SHERWIN, S. J. 2008 Convective instability and transient growth in flow over a backward-facing step. *J. Fluid Mech.* **603**, 271–304.

BLACKBURN, H. M. & SHERWIN, S. J. 2004 Formulation of a Galerkin spectral element–Fourier method for three-dimensional incompressible flows in cylindrical geometries. *J. Comput. Phys.* **197** (2), 759–778.

BOIKO, A., DOVGAL, A. & SOROKIN, A. 2012 Instability of a backward-facing step flow modified by stationary streaky structures. *Phys. Fluids* **24**, 104104.

BOTTARO, A., CORBETT, P. & LUCHINI, P. 2003 The effect of base flow variation on flow stability. *J. Fluid Mech.* **476**, 293–302.

BRANDT, L., SIPP, D., PRALITS, J. O. & MARQUET, O. 2011 Effects of base-flow variation in noise amplifiers: the flat-plate boundary layer. *J. Fluid Mech.* **687**, 503–528.

CATHALIFAUD, P. & LUCHINI, P. 2000 Algebraic growth in boundary layers: optimal control by blowing and suction at the wall. *Eur. J. Mech. (B/Fluids)* **19**, 469–490.

CHOMAZ, JM 2005 Global instabilities in spatially developing flows: Non-normality and nonlinearity. *Annu. Rev. Fluid Mech.* **37**, 357–392.

GAVARINI, M. I., BOTTARO, A. & NIEUWSTADT, F. T. M. 2004 The initial stage of transition in pipe flow: role of optimal base-flow distortion. *J. Fluid Mech.* **517**, 131–165.

GIANNETTI, F. & LUCHINI, P. 2007 Structural sensitivity of the first instability of the cylinder wake. *J. Fluid Mech.* **581**, 167–197.

GUÉGAN, A., SCHMID, P. & HUERRE, P. 2006 Optimal energy growth and optimal control in swept hiemenz flow. *J. Fluid Mech.* **566**, 11–45.

HUERRE, P. & MONKEWITZ, P. A. 1990 Local and global instabilities in spatially developing flows. *Annu. Rev. Fluid Mech.* **22**, 473–537.

KAIKTSIS, L, KARNIADAKIS, G. & ORSZAG, S. 1996 Unsteadiness and convective instabilities in two-dimensional flow over a backward-facing step. *J. Fluid Mech.* **321**, 157–187.

KAIKTSIS, L. & MONKEWITZ, P. 2003 Global destabilization of flow over a backward-facing step. *Phys. Fluids* **15**, 3647.

KALTENBACH, H. & JANKE, G. 2000 Direct numerical simulation of flow separation behind a swept, rearward-facing step at Re_H=3000. *Phys. Fluids* **12**, 2320–2337.

KARNIADAKIS, G. E., ISRAELI, M. & ORSZAG, S. A. 1991 High–order splitting methods for the incompressible Navier–Stokes equations. *J. Comput. Phys.* **97** (2), 414–443.

LANZERSTORFER, D. & KUHLMANN, H. 2012 Global stability of the two-dimensional flow over a backward-facing step. *J. Fluid Mech.* **693**, 1–27.

LASHGARI, IMAN, TAMMISOLA, OUTI, CITRO, VINCENZO, JUNIPER, MATTHEW & BRANDT, LUCA 2014 The planar x-junction flow: stability analysis and control. *J. Fluid Mech.* **753**, 1–28.

LE, H., MOIN, P. & KIM, J. 1997 Direct numerical simulation of turbulent flow over a backward-facing step. *J. Fluid Mech.* **330**, 349–374.

LESSHAFFT, L. & MARQUET, O. 2010 Optimal velocity and density profiles for the onset of absolute instability in jets. *J. Fluid Mech.* **662**, 398–408.

MAO, X., BLACKBURN, H. M. & SHERWIN, S. J. 2012 Optimal inflow boundary condition perturbations in steady stenotic flows. *J. Fluid Mech.* **705**, 306–321.

MAO, X., BLACKBURN, H. M. & SHERWIN, S. J. 2013 Calculation of global optimal initial and boundary perturbations for the linearised incompressible Navier–Stokes equations. *J. Comput. Phys.* **235**, 258–273.

MARQUET, O., SIPP, D., CHOMAZ, J. M & JACQUIN, L. 2008a Amplifier and resonator dynamics of a low-reynolds-number recirculation bubble in a global framework. *J. Fluid Mech.* **605**, 429–443.

MARQUET, O., SIPP, D. & JACQUIN, L. 2008b Sensitivity analysis and passive control of cylinder flow. *J. Fluid Mech.* **615**, 221–252.

MCGREGOR, O. & WHITE, R. 1970 Drag of rectangular cavities in supersonic and transonic flow including the effects of cavity resonance. *AIAA J.* **8**, 1959–1964.

MÉTAIS, O. 2001 *Large-eddy simulation of turbulence. In New Trends in Turbulence*. Springer.

PARK, H., JEON, W., CHOI, H. & YOO, J. 2007 Mixing enhancement behind a backward-facing step using tabs. *Phys. Fluids* **19**, 105103.

PRADEEP, D. S. & HUSSAIN, F. 2006 Transient growth of perturbations in a vortex column. *J. Fluid Mech.* **550**, 251–288.

SCHÄFER, F., BREUER, M. & DURST, F. 2009 The dynamics of the transitional flow over a backward-facing step. *J. Fluid Mech.* **623**, 85–119.

SCHMID, PETER J. 2007 Nonmodal stability theory. *Annu. Rev. Fluid Mech.* **39**, 129–162.

SCHRADER, L., BRANDT, L. & HENNINGSON, D. S. 2009 Receptivity mechanisms in three-dimensional boundary-layer flows. *J. Fluid Mech.* **618**, 209–241.

STRYKOWSKI, P. J. & SREENIVASAN, K. R. 1990 On the formation and suppression of vortex shedding at low reynolds numbers. *J. Fluid Mech.* **218**, 71–107.

TREFETHEN, LLOYD N., TREFETHEN, ANNE E., REDDY, SATISH C. & DRISCOLL, TOBIN A. 1993 Hydrodynamic stability without eigenvalues. *Science* **261**, 578–584.

VANNESTE, J. 1999 A spatial analogue of transient growth in plane Couette flow. *J. Fluid Mech.* **397**, 317–330.

WEE, D., YI, T., ANNASWAMY, A. & GHONIEM, A. 2004 Self-sustained oscillations and vortex shedding in backward-facing step flows: Simulation and linear instability analysis. *Phys. Fluids* **16**, 3361.

YANASE, S., KAWAHARA, G. & KIYAMA, H. 2001 Three-dimensional vortical structures of a

backward-facing step flow at moderate reynolds numbers. *J. Phys. Soc. Japan* **70**, 3550–3555.

YOKOYAMA, H., TSUKAMOTO, Y., KATO, C. & IIDA, A. 2007 Self-sustained oscillations with acoustic feedback in flows over a backward-facing step with a small upstream step. *Phys. Fluids* **19**, 106104.

ZAKI, T. A., WISSINK, J. G., RODI, W. & DURBIN, P. A. 2010 Direct numerical simulations of transition in a compressor cascade: the influence of free-stream turbulence. *J. Fluid Mech.* **665**, 57–98.

ZHANG, H., FAN, B. & CHEN, Z. 2010 Optimal control of cylinder wake flow by electro-magnetic force based on adjoint flow field **29**, 53–60.